MICROCOPY RESOLUTION TEST CHART

NATIONAL BUREAU OF STANDARDS-1963-A

High Order Nonlinear Finite Element
Analysis of the Axisymmetric Rubber
Membrane

Arthur Johnson[*]

Isaac Fried[**]

Boston University
Department of Mathematics
Boston, Mass. 02215

JAN 2 5 1984

A

[*]Graduate student (Engineer at NARADCOM
ILIR project A91A, Department of the Army)

[**]Associate Professor

84 01 24   022

REPORT DOCUMENTATION PAGE		READ INSTRUCTIONS BEFORE COMPLETING FORM
1. REPORT NUMBER BU 6 - 80	2. GOVT ACCESSION NO.	3. RECIPIENT'S CATALOG NUMBER
4. TITLE (and Subtitle) High Order Nonlinear Finite Element Analysis of the Axisymmetric Rubber Membrane.		5 TYPE OF REPORT & PERIOD COVERED Technical Report
		6. PERFORMING ORG. REPORT NUMBER
7. AUTHOR(s) Arthur Johnson & Isaac Fried		8. CONTRACT OR GRANT NUMBER(s) ILIR-A91A DOA ONR-Nooo14-76C-036
9. PERFORMING ORGANIZATION NAME AND ADDRESS Boston University, Department of Mathematics Boston, MA 02215		10. PROGRAM ELEMENT, PROJECT, TASK AREA & WORK UNIT NUMBERS
11. CONTROLLING OFFICE NAME AND ADDRESS Office of Naval Research Arlington, VA		12. REPORT DATE
		13. NUMBER OF PAGES
14. MONITORING AGENCY NAME & ADDRESS(If different from Controlling Office) As Above		15. SECURITY CLASS. (of this report)
		15a. DECLASSIFICATION DOWNGRADING SCHEDULE Unclassified

16. DISTRIBUTION STATEMENT (of this Report)

Distribution Unlimited

17. DISTRIBUTION STATEMENT (of the abstract entered in Block 20, If different from Report)

18. SUPPLEMENTARY NOTES

19. KEY WORDS (Continue on reverse side if necessary and identify by block number)

Finite Elements, Nonlinear Mechanics, Rubber membrane, Numerical integration, Newton Raphson method.

20. ABSTRACT (Continue on reverse side if necessary and identify by block number)

The nonlinear deformations of axisymmetric membranes made of Mooney material are determined using the finite element method. The analysis is constructed in a form that can be easily extended to other nonquadratic energy functionals encountered in finite elasticity. The axisymmetric deformations analysed are the in-plane expansion of a disk with a hole, the inflation of an initially flat circular disk, the out-of-plane deformation of a disk with an inclusion caused by moving the inclusion along the axis

DD FORM 1473 1 JAN 73   EDITION OF 1 NOV 65 IS OBSOLETE

20. of symmetry, and the inflation of a torus with both circular and elliptical cross sections. Stability of the solutions obtained is verified by computing the eigenspectrum of the potential energy's Hessian. Convergence rates with respect to mesh reduction are numerically determined for the displacement field and the strain energy. Quadratic three node Lagrange elements are used for all problems except the torus for which cubic Hermite elements are also used.

A-1

TABLE OF CONTENTS

TABLE OF CONTENTS - CONTINUED

LIST OF TABLES

LIST OF ILLUSTRATIONS

LIST OF ILLUSTRATIONS - CONTINUED

SYMBOLS

$\{\cdot\}$ a vector or a finite set

$[\cdot]$ a matrix

$\|\cdot\|$ l_2 norm of a vector

λ_i stretch ratio associated with the coordinate direction i, the length of an infinitesimal line element after deformation divided by the undeformed infinitesimal line element length

I_i strain invariant i

U strain energy, the energy contained in the deformed membrane

μ strain energy per unit volume, $U = \int \mu \, dv$

W total work done by the applied forces

$\Pi(\{u\})$ total potential energy functional, $\Pi = U - W$

$\Pi_e(\{u\}_e)$ potential energy functional for element e, $\Pi = \sum \Pi_e$

$\{u\}_e$ finite element nodal variables for element e

$\{u\}_{er}$ reduced set of nodal variables for element e, obtained when constraints on an element's nodal variables are enforced

$\{u\}$ union of all element nodal variables, the finite element global displacement vector

SYMBOLS - CONTINUED

$\{g\}_e$ — gradient of element e's potential energy functional, $\dfrac{\partial \pi}{\partial \{u\}_e^T}$

$\{g\}$ — union of all element gradients, $\overset{N}{\underset{e=1}{\bigcup}} \{g\}_e$

$[k]_e$ — Hessian of element e's potential energy functional, $\dfrac{\partial^2 \pi}{\partial \{u\}_e \partial \{u\}_e^T}$

$[k]$ — union of all element Hessians, $\overset{N}{\underset{e=1}{\bigcup}} [k]_e$

$[c]_e$ — matrix used to express equations of constraint in en element, $\{u\}_e = [c]_e \{u\}_{er}$

x, y — undeformed coordinates of the membrane in the reference rectangular coordinate system

R, ω — global parametric coordinates

ξ, Ω — element parametric coordinates

X, Y — deformed coordinates of the membrane in the reference rectangular coordinate system, $X = X(R)$

$\tilde{X}, \tilde{Y}$ — finite element approximations to X and Y

$\{\varphi\}, \{\psi\}$ — interpolation functions used to generate the finite element approximations $\tilde{X}$ and $\tilde{Y}$,
$$\tilde{X} = \{\varphi\}^T \{u\}_e \quad \text{and} \quad \tilde{Y} = \{\psi\}^T \{u\}_e$$

$(\cdot)'$ — differentiation with respect to a global parameter, $\tilde{X}' = \dfrac{d\tilde{X}}{dR}$

SYMBOLS - CONTINUED

$\dot{(\cdot)}$ differentiation with respect to an element parameter, $\dot{\hat{X}} = \dfrac{d\,\hat{X}}{d\,\xi}$

$\doteq$ approximately equal to

CHAPTER 1

INTRODUCTION

The finite element method is a numerical analysis technique which can be used to find the location in N-space at which some scalar functional of N variables is stationary. This method is one of the most popular methods used to find solutions of both linear and nonlinear problems in the theory of elasticity. Finite element techniques which allow for a systematic check on convergence with respect to mesh size, discretization accuracy, are useful to the numerical analyst. The accumulation of round-off errors and the errors made when numerical integration is used can destroy the accuracy of a finite element algorithm. In the case of nonlinear elasticity the round-off and integration errors can be magnified because of the incremental techniques used. When the deformations in an elastic body are small and when the material properties are not dependent on the deformation then the use of the finite element method leads to an energy functional, the discrete energy functional, which is quadratic in N-space. The first variation of this functional leads to a set of linear equations. The solution of these equations gives the point in N-space where the functional is stationary. If the material properties are dependent on the deformation or if the deformations are large then the discrete

energy functional is not quadratic in N-space. The first variation of the energy functional then leads to a nonlinear set of equations. The solutions of these equations represent the stationary points in N-space where the discrete functional is stationary. Since there may be more than one solution the stability of the discrete energy functional at these points becomes important. Solutions of interest, stable points, are those points in N-space for which the discrete energy functional is a local minimum. Stability in N-space requires that the Hessian of the discrete energy functional be positive definite at a solution point.

1.1 The Energy Functional for Finite Deformations of Mooney Materials.

A historical account of the development of the first energy expressions used in the analysis of rubber materials is given in Treloar's[1] book on rubber elasticity. Due to the fact that vulcanized rubber consists of long molecules linked together to form an irregular three-dimensional network early researchers developed methods for describing the behavior of a large assembly of elastic links. As described by Treloar these theories were developed during the period from 1936 to 1947. The problem of determining physical variables to describe the energy functional was resolved when a theory was developed to describe the pure homogeneous strain deformation of rubber by

characterizing the strain in terms of three principal extension ratios λ_1, λ_2, and λ_3 along three mutually perpendicular axes. A brief summary of Treloar's description of this theory is given here.

Definition (D.1): Pure homogeneous strain and principal stretch ratios λ_1, λ_2, λ_3;

Pure homogeneous strain exists when a unit cube in the undeformed body is transformed into a rectangular parallelepiped having three unequal edge lengths λ_1, λ_2, and λ_3. See Figure 1.1. The deformed edge lengths λ_1, λ_2, and λ_3 are called the principal stretch ratios.

Definition (D.2): Strain invariants I_1, I_2, and I_3.

$$I_1 = \lambda_1^2 + \lambda_2^2 + \lambda_3^2$$
$$I_2 = \lambda_1^2\lambda_2^2 + \lambda_2^2\lambda_3^2 + \lambda_3^2\lambda_1^2 \qquad (1.1.1)$$
$$I_3 = \lambda_1^2\lambda_2^2\lambda_3^2$$

Assumption (A.1): The material is assumed to be isotropic in the unstressed state and incompressible in all states of deformation.

The requirement that the pure homogeneous deformation be incompressible implies that $\lambda_1\lambda_2\lambda_3 = 1$ or that

UNDEFORMED

DEFORMED

λ_1

λ_2

λ_3
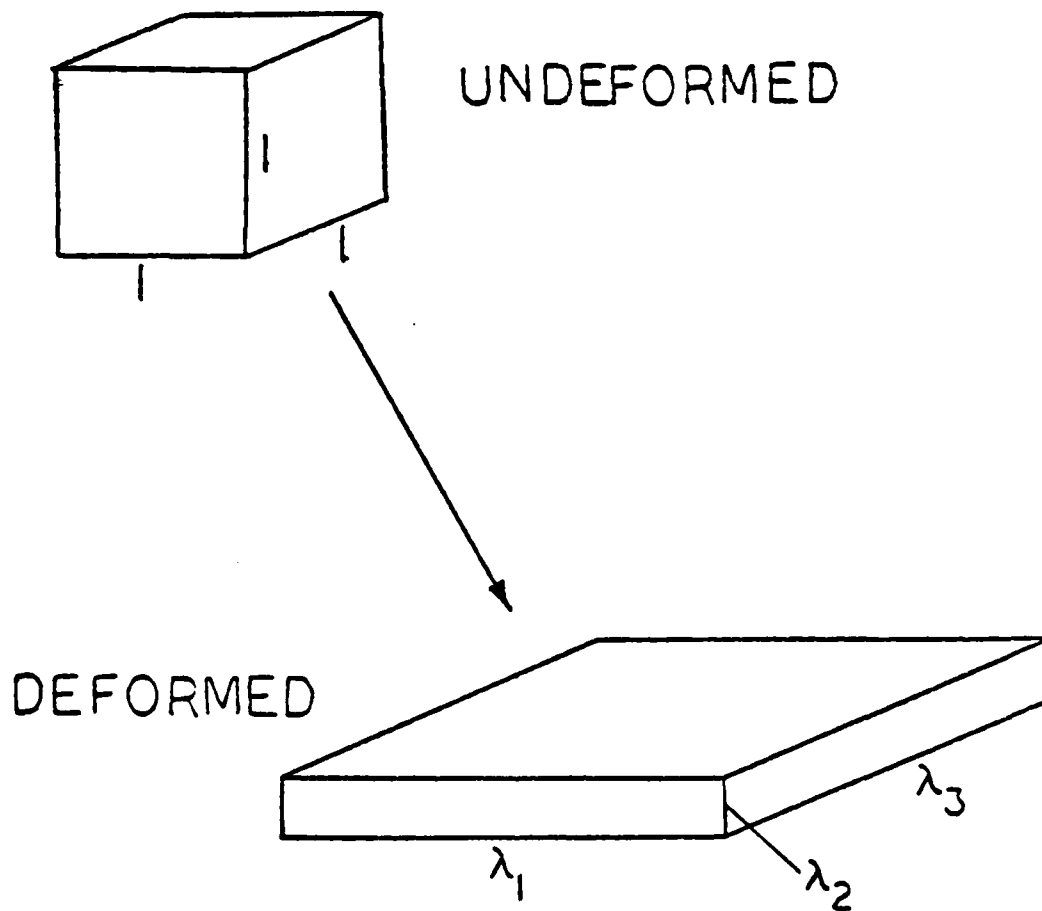
FIGURE 1.1   A PURE HOMOGENEOUS
STRAIN DEFORMATION

$$I_3 = \lambda_1^2 \lambda_2^2 \lambda_3^2 = 1 \qquad (1.1.2)$$

Then, for an incompressible material there are only two stretch ratios that are a function of the deformation, I_1 and I_2. Using (1.1.2) in (1.1.1) we have

$$I_1 = \lambda_1^2 + \lambda_2^2 + \frac{1}{\lambda_1^2 \lambda_2^2}$$

$$\qquad (1.1.3)$$

$$I_2 = \lambda_1^2 \lambda_2^2 + \frac{1}{\lambda_1^2} + \frac{1}{\lambda_2^2}$$

The strain energy density functional, μ, for a material satisfying D.1, D.2, and A.1 is given by

$$\mu = \sum_{i=0}^{\infty} \sum_{j=0}^{\infty} C_{ij} (I_1 - 3)^i (I_2 - 3)^j \qquad (1.1.4)$$

where $C_{oo} = 0$

C_{ij} are material constants.

The most common form of (1.1.4) used in the analysis of finite deformations of incompressible materials is the Mooney[2,3,4] form which is given as follows.

$$\mu = C_1 \left[(I_1 - 3) + \alpha (I_2 - 3) \right] \qquad (1.1.5)$$

There are other formulations for finite deformations of incompressible materials. Recently Cescotto and Fonder[5] have summarized these formulations. Their work is concerned with variational principles which allow for a more general behavior of the material than the Mooney formulation allows for. Oden and Key[6] have considered the effects of using different energy functions in finite elasticity. They noticed that by using different strain energy functions, related to the Mooney form, solutions are obtained which are significantly different. We are concerned with the effect of numerical integration and mesh refinement on the solutions to problems with a given strain energy formulation. The formulation chosen here is one of minimum potential energy using the Mooney form for the strain energy. This formulation has been shown to be meaningful by Tielking and Feng[7]. They analyzed nonlinear axisymmetric membrane problems by applying the Ritz method to the total potential energy functional, $\prod$, given as follows

$$\prod = \int_V \mu \, dv - W \qquad (1.1.6)$$

where V = the volume of the undeformed elastic body

and W = the work done by the applied fractions.

We will be concerned here with the discretization of this functional

by the finite element method. The objective being to computationally determine the effects of numerical integration and mesh refinement on the accuracy of the finite element solutions.

1.2 The Finite Element Method.

We are concerned here with the displacement finite element method. The theoretical development of the finite element method for both linear and nonlinear problems of elasticity has been extensively researched and documented. A detailed description of this technique can be found in books by Oden[4], and Strang and Fix[8]. We present here a summary of the finite element method as it applies to this study. The technique presented for numerically evaluating the element matrices is suitable for evaluating the effects of numerical integration on the accuracy of the finite element solutions.

Consider an integral functional on (0, 1) of the following form.

$$I(u) = \int_0^1 F(x, u, u') \, dx \qquad (1.2.1)$$

F may contain rational expressions of u, u' or their powers. Partition of the interval (0, 1) into N subintervals (x_i, x_{i+1}) where the points x_i, $i = 1, 2, \cdots, N+1$ are called the nodes. Define a set of variables $\{\tilde{u}_i, \tilde{u}_i'\}$ which are the finite element approximations to u and its derivatives at the set of nodes $\{x_i\}$. That is, $\tilde{u}_i$ is the approximation to u at node i located at x_i. We now wish to approximate u between the nodes by polynomial interpolation which is completely defined by the nodal variables $\{\tilde{u}_i, \tilde{u}_i'\}$.

The power of the finite element method lies in the next step. A low
order interpolation, usually between 1st and 5th, is chosen for the
interpolation. This requires the polynomials to be locally defined
over intervals associated with a small number of nodal variables which
define the coefficients of the polynomials. These intervals or groups
of intervals ($(e), e = 1, \cdots, N_e$) are called elements. When
this procedure is followed an approximation to the integral (1.2.1) is
available in the following form.

$$\tilde{\tilde{I}}(\tilde{u}) = \int_0^1 F(\varkappa, \tilde{u}, \tilde{u}') d\varkappa \qquad (1.2.2)$$

or

$$\hat{\tilde{I}}(\hat{u}) = \sum_{e=1}^{N_e} \int_{(e)} F(\varkappa, \hat{u}, \tilde{u}') d\varkappa \qquad (1.2.3)$$

$\hat{\tilde{I}}(\hat{u})$ is the approximation to $I(u)$. The desired functions
$u(\varkappa)$ are those which make $I(u)$ stationary. The displacement
finite element solutions for a given partition and interpolation order
are found by using the calculus of variations to determine, of all

possible nodal values $\left\{ \widetilde{u}_i, \widetilde{u}_i' \right\}$ which set makes $\widehat{\widetilde{I}(\widetilde{u})}$ station-

ary. Thus, the variational boundary conditions must be enforced on

the finite element approximation. This is usually a trivial task since

the finite element approximation functions, as described above, are

locally defined and modifications need be made only over a few

elements. The form of the finite element approximation for elements

not on the boundary remains unchanged.

If the partition is allowed to become successively finer then the

accuracy of the finite element approximations increases (until com-

putational errors arise). The accuracy and rate of convergence of the

finite element approximations when the partition is refined is a

function of the order of interpolation chosen in elliptic boundary

value problems. The use of higher order interpolations (quadratic,

cubic, quintic) in linear elliptic problems often proves useful. In

the problems studied in this dissertation $I(u)$ does not have an

associated linear elliptic differential operator and the rates of con-

vergence are not known in terms of parameters characterizing a dif-

ferential operator.

Consider the discrete integral functional given by (1.2.3). Con-

struct a uniform partition of (0, 1) such that the intervals of the

possible nodal values $\left\{ \tilde{u}_i, \tilde{u}_i' \right\}$ which set makes $\tilde{\tilde{I}}(\tilde{u})$ station-

ary. Thus, the variational boundary conditions must be enforced on

the finite element approximation. This is usually a trivial task since

the finite element approximation functions, as described above, are

locally defined and modifications need be made only over a few

elements. The form of the finite element approximation for elements

not on the boundary remains unchanged.

If the partition is allowed to become successively finer then the

accuracy of the finite element approximations increases (until com-

putational errors arise). The accuracy and rate of convergence of the

finite element approximations when the partition is refined is a

function of the order of interpolation chosen in elliptic boundary

value problems. The use of higher order interpolations (quadratic,

cubic, quintic) in linear elliptic problems often proves useful. In

the problems studied in this dissertation $I(u)$ does not have an

associated linear elliptic differential operator and the rates of con-

vergence are not known in terms of parameters characterizing a dif-

ferential operator.

Consider the discrete integral functional given by (1.2.3). Con-

struct a uniform partition of (0, 1) such that the intervals of the

partition can be grouped into elements with the same number of nodal variables. Then, $\tilde{u}(x)$ can be expressed as follows.

$$\tilde{u}(x) = \left\{ \varphi(x) \right\}^T \left\{ u \right\}_e \tag{1.2.4}$$

where $\left\{ \varphi(x) \right\}$ = a vector of interpolation functions

and $\left\{ u \right\}_e = \left\{ \tilde{u}_i , \tilde{u}'_i \right\}$ = a vector of the element nodal variables. Substitution of (1.2.4) into (1.2.3) leads to the following expression

$$\tilde{I}(\{u\}) = \sum_{e=1}^{N_e} \int_{(e)} F(x, \{u\}_e) \, dx \tag{1.2.5}$$

where $\left\{ u \right\} = \bigcup_{e=1}^{N_e} \left\{ u \right\}_e .$

The condition that (1.2.5) be stationary is given by $\delta \tilde{I} = 0$ or

$$\sum_{e=1}^{N_e} \{\delta u\}^T \left\{ \int_{(e)} \frac{\partial F}{\partial \{u\}_e^T} \, dx \right\} = 0 \tag{1.2.6}$$

where $\left\{ \delta u \right\}_e$ = the variation of the element nodal variables.

Then, $\displaystyle\sum_{e=1}^{N_e} \left\{ \delta u \right\}_e^T \left\{ g \right\}_e = \left\{ \delta u \right\}^T \left\{ \bar{g} \right\} = 0$ \hfill (1.2.7)

where $\left\{ g \right\}_e = \displaystyle\int_{(e)} \frac{\partial F}{\partial \{u\}_e^T} \, d\not\!x$ = the element gradient vector

$\left\{ g \right\} = \displaystyle\bigcup_{e=1}^{N_e} \left\{ g \right\}_e$ = the global gradient vector

and $\left\{ \delta u \right\} = \displaystyle\bigcup_{e=1}^{N_e} \left\{ \delta u \right\}_e$ = the global variation of nodal

variables. Since $\left\{ \delta u \right\}^T$ is arbitrary except for the constraints

we have the following condition on $\left\{ u \right\}$ at a stationary location

of $\tilde{I}(\{u\})$.

$$\left\{ g \right\} = \left\{ 0 \right\} \hspace{3cm} (1.2.8)$$

When finding the solution to (1.2.8) and when checking the stability

of the stationary point the Hessian, $[k]$, of $\tilde{I}(\{u\})$ is

often used. It is given as follows.

$$[k] = \frac{\partial\{g\}}{\partial\{u\}} \qquad (1.2.9)$$

The Hessian is computed on an element bases as shown below

$$[k] = \bigcup_{e=1}^{N_e} [k]_e = \bigcup_{e=1}^{N_e} \frac{\partial[g]_e}{\partial\{u\}_e^T} \qquad (1.2.10)$$

1.3 The Use of Numerical Integration to Obtain Element Matrices.

Numerical integration is used in the finite element method when exact integration is not practical. This is the case when high order interpolation is assumed, when multi-dimensional curved elements are used, and when the integral functional is not a polynomial in the finite element nodal variables. Strang and Fix[8] state the fundamental problem as follows: "What degree of accuracy in the integration formula is required for convergence? It is not required that every polynomial which appears be integrated exactly." This question was answered for elliptic problems of 2mth order by Fried[9] in 1974. The requirement for elliptic problems is that the terms in the

integral functional should be integrated by a rule which is exact for polynomials of degree 2(p-m) where m is the highest order derivative appearing in the integral functional and p is the order of the interpolation polynomials. If we tried to extend this idea to the case when the integral functional contains rational expressions of $u(x)$ and $u'(x)$ then we would require exact integration to some as yet undetermined order of the rational expressions. Such a requirement would be strict and may lead to an expensive integration routine. Also, such a requirement may not even make sense. For example, the errors involved in assuming the solution is a polynomial (the interpolation assumption) may be larger than the errors introduced by inexactly integrating the rational expressions in the integral functional $\tilde{I}(\{u\})$ with a low order scheme. In this study problems with rational expressions in the energy integral are solved by the finite element method with low order integration schemes. The effects of increasing the order of accuracy of the integration schemes are presented.

Let $x = F_e(\xi)$ be a mapping of the interval (e) onto the interval (-1, 1). Then the element gradient and Hessian matrices can be numerically computed as follows.

$$\{q\}_e = \sum_{j=1}^{P} \omega_j \left. \frac{\partial F(\xi, \{u\}_e)}{\partial \{u\}_e^T} \right|_{\xi = \xi_j} \dot{F}(\xi_j) \qquad (1.3.1)$$

and

$$[k]_e = \sum_{j=1}^{P} \omega_j \left. \frac{\partial^2 F(\xi, \{u\}_e)}{\partial \{u\}_e \, \partial \{u\}_e^T} \right|_{\xi = \xi_j} \dot{F}(\xi_j) \qquad (1.3.2)$$

where $\quad j = 1, 2, \cdots, P$

$\qquad P = $ the number of integration points

$\qquad \xi_j = $ the jth integration point in $(-1, 1)$

$\qquad \omega_j = $ the weight at the jth integration point.

This integration technique has recently been applied by Fried[10] to the nonlinear finite element analysis of cantilever beams and plates. Element matrices containing rational expressions of the nodal variables were evaluated with a low order integration scheme. The rank of the element Hessian was reduced but when the boundary conditions were applied a full rank global Hessian was obtained. In this study we will determine numerically when the rank of the element and global Hessians

are reduced.

1.4 Newton's Method and the Incremental Loading

Formulation.

The method used to determine the solution to the nonlinear

equations given by (1.2.8) is a sequential method and is called

Newton's method. Given an initial vector $\{u\}_0$ the method computes

a series of vectors $\{u\}_1, \{u\}_2, \cdots$ which converge to a vector

$\{u\}_*$ for which $\{g(\{u\}_*)\} = \{0\}$. It is necessary that the

initial guess vector $\{u\}_0$ be close enough to $\{u\}_*$ for a two

term Taylor expansion of $\{g\}$ to be approximately valid. For this

reason a modification of the method, called the incremental loading

formulation, is used when it is difficult to estimate a good starting

point $\{u\}_0$. Newton's method can be described by considering a

Taylor expansion of $\{g\}$ at the Nth vector of the series. This is

given as follows

$$\{g\}_{N+1} \doteq \{g\}_N + [k]_N \left\{ \{u\}_{N+1} - \{u\}_N \right\} . \qquad (1.4.1)$$

Requiring $\{g\}_{N+1}$ to be zero and assuming $[k]_N$ is not

singular we have Newton's method (1.4.2) for generating the series

which converges to $\{u\}_*$.

$$\{u\}_{N+1} = \{u\}_N - [k]_N^{-1}\{g\}_N \tag{1.4.2}$$

When the solution is dependent on a parameter, P , which may be large it is often possible to determine useful initial vectors $\{u\}_0$ only when P is small. In finite elasticity P is the loading. If the loading is large Newton's method is modified by finding the solution for a small load P_1 and using this solution as an initial guess for loading $P_2 = P_1 + \Delta P$ where ΔP is a small loading increment. This process is continued until the solution at

$$P = P_N = P_{N-1} + \Delta P$$ is obtained. This modification of

Newton's method is called an incremental loading formulation.

Other methods can be used to obtain solutions to (1.2.8). Both random searches and gradient techniques are popular alternatives. Also, Newton's method as described above can be improved[11] but the algorithms described here worked well on the problems solved in this study. A more detailed discussion of techniques for solving nonlinear equations in N-dimensional spaces is available in Oden's[4] book.

1.5 Evaluation of the Effects of Numerical Integration.

The finite element method is capable of dealing with complex domains in the analysis of both linear and nonlinear boundary value problems. A computational evaluation of the use of numerical integration in the finite element analysis of incompressible membranes is important to the numerical analyst. The results, not predictable a-priori, determine the advantages and disadvantages of using certain orders of numerical integration to compute finite element matrices. The results are presented in a manner which distinguishes errors from discretization from those of integration allowing practical orders of integration to be determined for several problems.

CHAPTER 2

FINITE ELEMENT ANALYSIS

2.1 The Potential Energy Functional for Axisymmetric Incompressible Membranes.

The stretch ratios for axisymmetric incompressible membranes take a form which allows for a general derivation of the finite element matrices (see Ref. 7). Coefficients in the derived form of the element matrices are specified by the particular axisymmetric problem chosen for analysis. Using the Mooney form (1.1.5) of the strain energy per unit volume with $C_1 = 1$ and using (1.1.6) we have the following form of the potential energy functional.

$$\Pi = \int_V \left[(I_1 - 3) + \alpha (I_2 - 3) \right] dV - W \qquad (2.1.1)$$

The geometry of axisymmetric membranes is shown in Figure 2.1. We assume the undeformed membrane is of unit thickness. There is no dependence on the variable Θ shown in Figure 2.1 so (2.1.1) becomes

$$\Pi = 2\pi \int_R \left[(I_1 - 3) + \alpha (I_2 - 3) \right] R \, dR - W \qquad (2.1.2)$$

AXIS OF SYMMETRY

(S,Y)

DEFORMED

λ_1

$d\theta$

λ_2

B'

A'

C'

C

B

A

$d\theta$

UNDEFORMED.

θ

(R,X)
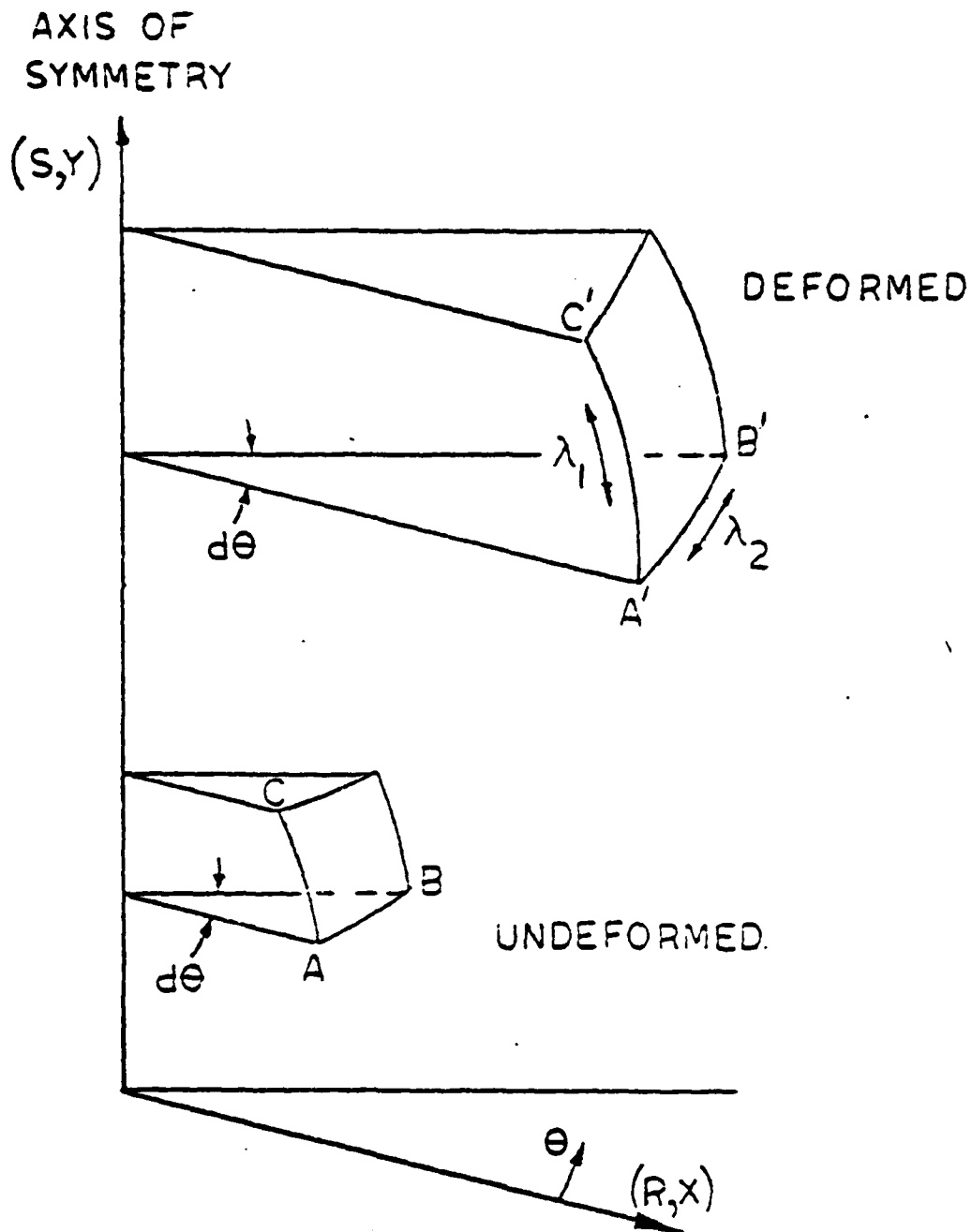
(R,S) = COORDINATES OF UNDEFORMED SURFACE
(X,Y) = COORDINATES OF DEFORMED SURFACE

FIGURE 2.1   GEOMETRY OF AXISYM-
METRIC MEMBRANES

The stretch ratios are given as follows.

$$\lambda_1 = \frac{A'B'}{AB} = \left(\frac{(X')^2 + (Y')^2}{1 + (S')^2} \right)^{1/2}$$

<div align="right">(2.1.3)</div>

$$\lambda_2 = \frac{A'C'}{AC} = \frac{X}{R}$$

where $\quad (\bullet)' = \dfrac{d(\bullet)}{dR}$

The domain of integration is now partitioned as described in section 1.2 and over each element of the domain we approximate X and Y in terms of the element nodal variables. Using the appropriate interpolation functions we have

$$\widetilde{X} = \{\varphi\}^T \{u\}_e$$

<div align="right">(2.1.4)</div>

and $\quad \widetilde{Y} = \{\psi\}^T \{u\}_e$

Using these approximations the squares of the stretch ratios become

$$\lambda_1^2 = \frac{\{u\}_e^T \left[\{\varphi'\}\{\varphi'\}^T + \{\psi'\}\{\psi'\}^T \right]\{u\}_e}{\Lambda}$$

(2.1.5)

$$\lambda_2^2 = \frac{\{u\}_e^T \left[\{\varphi\}\{\varphi\}^T \right]\{u\}_e}{R^2}$$

where $\quad \Lambda = 1 + (S')^2$

Mapping the element onto the interval (-1, 1) with the relation

$R = F(\xi)$, using the expression (1.1.3) for the strain

invariants I_1 and I_2 , and using numerical integration at

p points ξ_i as described in section 1.3 we arrive at the fol-

lowing form of the discrete potential energy.

$$\Pi = \sum_{e=1}^{N_e} \Pi_e$$

(2.1.6)

where

$$\Pi_e = 2\pi \sum_{i=1}^{P} w_i F_i \dot{F}_i \left(\left(\Lambda_i^{-1} \dot{F}_i^{-2} \{u\}_e^T \left[\{\dot{\varphi}_i\}\{\dot{\varphi}_i\}^T + \{\dot{\psi}_i\}\{\dot{\psi}_i\}^T \right]\{u\}_e \right.$$

$$+ \bar{F}_i^{-2} \{u\}_e^T \left[\{\varphi_i\}\{\varphi_i\}^T \right] \{u\}_e$$

$$+ \frac{\Lambda_i F_i^2 \dot{F}_i^2}{\left(\{u\}_e^T \left[\{\dot{\varphi}_i\}\{\dot{\varphi}_i\}^T + \{\psi_i\}\{\psi_i\}^T \right] \{u\}_e \right)\left(\{u\}_e^T \left[\{\varphi_i\}\{\varphi_i\}^T \right] \{u\}_e \right)} - 3 \Bigg)$$

$$+ \alpha \left(\Delta_i^{-1} \bar{F}_i^{-2} \bar{F}_i^{-2} \left(\{u\}_e^T \left[\{\dot{\varphi}_i\}\{\dot{\varphi}_i\}^T + \{\psi_i\}\{\psi_i\}^T \right] \{u\}_e \right)\left(\{u\}_e^T \left[\{\varphi_i\}\{\varphi_i\}^T \right] \{u\}_e \right) \right.$$

$$+ \frac{\Lambda_i \dot{F}_i^2}{\{u\}_e^T \left[\{\dot{\varphi}_i\}\{\dot{\varphi}_i\}^T + \{\psi_i\}\{\psi_i\}^T \right] \{u\}_e}$$

$$+ \frac{F_i^2}{\{u\}_e^T \left[\{\varphi_i\}\{\varphi_i\}^T \right] \{u\}_e} - 3 \Bigg)\Bigg) - W_e$$

and W_e = the term associated with the work done by the applied tractions.

2.2 The Element Gradient.

The expression for the total potential energy can be changed into a form which is more convenient for computing the gradient. The stretch ratios λ_1 and λ_2 in an element are expressed in terms of three functions of ξ. These expressions are given below.

$$A(\xi, \{u\}_e^T) = \{u\}_e^T \{\dot{\varphi}(\xi)\} = \{\dot{\varphi}(\xi)\}^T \{u\}_e = A(\xi, \{u\}_e)$$

$$B(\xi, \{u\}_e^T) = \{u\}_e^T \{\dot{\psi}(\xi)\} = \{\dot{\psi}(\xi)\}^T \{u\}_e = B(\xi, \{u\}_e) \qquad (2.2.1)$$

$$C(\xi, \{u\}_e^T) = \{u\}_e^T \{\varphi(\xi)\} = \{\varphi(\xi)\}^T \{u\}_e = C(\xi, \{u\}_e)$$

Using (2.2.1) the stretch ratios λ_1 and λ_2 become

$$\lambda_1 = \left(\frac{A^2 + B^2}{\Lambda} \right)^{1/2} \qquad . \qquad (2.2.2)$$

$$\lambda_2 = \frac{C}{R}$$

The total potential energy expressed in terms of A, B, and C is obtained by substituting (2.2.1) into (2.1.6). We obtain the following expression for Π_e.

$$\Pi_e = 2\pi \sum_{i=1}^{P} \omega_i F_i \dot{F}_i \left(\left(\Delta_i^{-1} \dot{F}_i^{-2} (A_i^2 + B_i^2) \right) + \dot{F}_i^{-2} C_i^2 \right.$$

$$+ \Delta_i F_i^2 \dot{F}_i^2 (A_i^2 + B_i^2)^{-1} C_i^{-2} - 3 \right)$$

$$\tag{2.2.3}$$

$$+ \alpha \left(\Delta_i^{-1} \dot{F}_i^{-2} F_i^{-2} (A_i^2 + B_i^2) C_i^2 + \Delta_i \dot{F}_i^2 (A_i^2 + B_i^2)^{-1} \right.$$

$$+ F_i^2 C_i^{-2} - 3 \right) \Bigg) - W_e$$

The element gradient is now found by differentiating (2.2.3) with respect to $\{u\}_e^T$. We have

$$\frac{\partial A(\xi, \{u\}_e^T)}{\partial \{u\}_e^T} = \{\dot{\varphi}(\xi)\}$$

$$\tag{2.2.4}$$

$$\frac{\partial B(\xi, \{u\}_e^T)}{\partial \{u\}_e^T} = \{\dot{\psi}(\xi)\}$$

$$\frac{\partial C(\xi, \{u\}_e^T)}{\partial \{u\}_e^T} = \{\varphi(\xi)\}$$

Using (2.2.4) we obtain, after simplification, the element gradient.

$$\{g\}_e = \frac{\partial \Pi_e}{\partial \{u\}_e^T}$$

$$\{g\}_e = 4\pi \sum_{i=1}^{P} \omega_i F_i \dot{F}_i \left(\right. \tag{2.2.5}$$

$$\{A_i \{\dot{\varphi}_i\} + B_i \{\dot{\psi}_i\}\} \left(1 + \alpha F_i^{-2} C_i^2\right) \left(\Lambda_i^{-1} F_i^{-2} - \Lambda_i \dot{F}_i^2 F_i^2 \left(A_i^2 + B_i^2\right)^{-2} C_i^2\right)$$

$$+ C_i \{\varphi_i\} \left(1 + \alpha \Lambda_i^{-1} \dot{F}_i^{-2} \left(A_i^2 + B_i^2\right)\right) \left(F_i^{-2} - \Lambda_i F_i^2 \dot{F}_i^2 \left(A_i^2 + B_i^2\right)^{-1} C_i^4\right) \right)$$

$$- \frac{\partial W_e}{\partial \{u\}_e^T}$$

2.3 The Element Hessian

The expression developed for the element gradient can be used to compute the element Hessian. We again use the expressions (2.2.1) to obtain

$$\frac{\partial A(\xi, \{u\}_e)}{\partial \{u\}_e} = \left\{\dot{\varphi}(\xi)\right\}^T$$

$$\tag{2.3.1}$$

$$\frac{\partial B(\xi, \{u\}_e)}{\partial \{u\}_e} = \left\{\dot{\psi}(\xi)\right\}^T$$

and
$$\frac{\partial C(\xi, \{u\}_e)}{\partial \{u\}_e} = \left\{ \varphi(\xi) \right\}^T$$

Substitution of (2.3.1) into (2.2.5), differentiation, and simplification leads to the element Hessian.

$$[k]_e = \frac{\partial \{g\}_e}{\partial \{u\}_e}$$

$$[k]_e = +\pi \sum_{i=1}^{P} \omega_i \, F_i \, \dot{F}_i \Bigg($$

$$\left(1 + \alpha \bar{F}_i^{-2} C_i^2 \right) \left(\Lambda_i^{-1} \dot{F}_i^{-2} - \Lambda_i \dot{F}_i^2 F_i^2 (A_i^2 + B_i^2)^{-2} C_i^{-2} \left(1 - 4 A_i^2 (A_i^2 + B_i^2)^{-1} \right) \right) \left[\{\varphi_i\} \{\varphi_i\}^T \right]$$

$$+ \left(1 + \alpha \bar{F}_i^{-2} C_i^2 \right) \left(\Lambda_i^{-1} \dot{F}_i^{-2} - \Lambda_i \dot{F}_i^2 F_i^2 (A_i^2 + B_i^2)^{-2} C_i^{-2} \left(1 - 4 B_i^2 (A_i^2 + B_i^2)^{-1} \right) \right) \left[\{\psi_i\} \{\psi_i\}^T \right]$$

$$+ \left(1 + \alpha \Lambda_i^{-1} \dot{F}_i^{-2} (A_i^2 + B_i^2) \right) \left(\dot{F}_i^2 + 3 \Lambda_i F_i^2 \dot{F}_i^2 (A_i^2 + B_i^2)^{-1} C_i^{-4} \right) \left[\{\varphi_i\} \{\varphi_i\}^T \right]$$

$$+ 2 A_i \left((A_i^2 + B_i^2)^{-2} C_i^{-3} \Lambda_i \dot{F}_i^2 F_i^2 + \alpha C_i \Lambda_i^{-1} \dot{F}_i^{-2} F_i^{-2} \right) \left[\{\varphi_i\} \{\psi_i\}^T + \{\psi_i\} \{\varphi_i\}^T \right]$$

$$+ 2 B_i \left((A_i^2 + B_i^2)^{-2} C_i^{-3} \Lambda_i \dot{F}_i^2 F_i^2 + \alpha C_i \Lambda_i^{-1} \dot{F}_i^{-2} F_i^{-2} \right) \left[\{\varphi_i\} \{\psi_i\}^T + \{\psi_i\} \{\varphi_i\}^T \right]$$

$$+ 4 A_i B_i C_i^{-2} (A_i^2 + B_i^2)^{-3} \Lambda_i \dot{F}_i^2 F_i^2 \left(1 + \alpha \bar{F}_i^{-2} C_i^2 \right) \left[\{\psi_i\} \{\psi_i\}^T + \{\psi_i\} \{\varphi_i\}^T \right] \Bigg)$$

$$- \frac{\partial^2 W_e}{\partial \{u\}_e \, \partial \{u\}_e^T}$$

(2.3.2)

2.4 Quadratic and Cubic Elements.

The particular forms of interpolation within an element can affect the results of an analysis. The quadratic three-node element and the cubic two-node elements were used in this study. The quadratic three-node element has only displacements for nodal variables and is a C^o element. The cubic two-node element has both displacements and first derivatives as nodal variables and is a C^1 element. These one-dimensional elements have interpolation functions related to Lagrange and Hermite polynomials. The quadratic element is called a second order Lagrange element and the cubic element is called a third order Hermite element.

The quadratic three-node element has the following set of nodal variables, see Figure 2.2.

$$\{u\}_e^T = \left\{ X_i, Y_i, X_{i+1}, Y_{i+1}, X_{i+2}, Y_{i+2} \right\}^T \tag{2.4.1}$$

The associated interpolation functions on (-1, 1) are

$$\{\varphi(\xi)\}^T = \left\{ \varphi_1(\xi), 0, \varphi_2(\xi), 0, \varphi_3(\xi), 0 \right\}^T \tag{2.4.2}$$

3 NODE QUADRATIC ELEMENT

2 NODE CUBIC ELEMENT
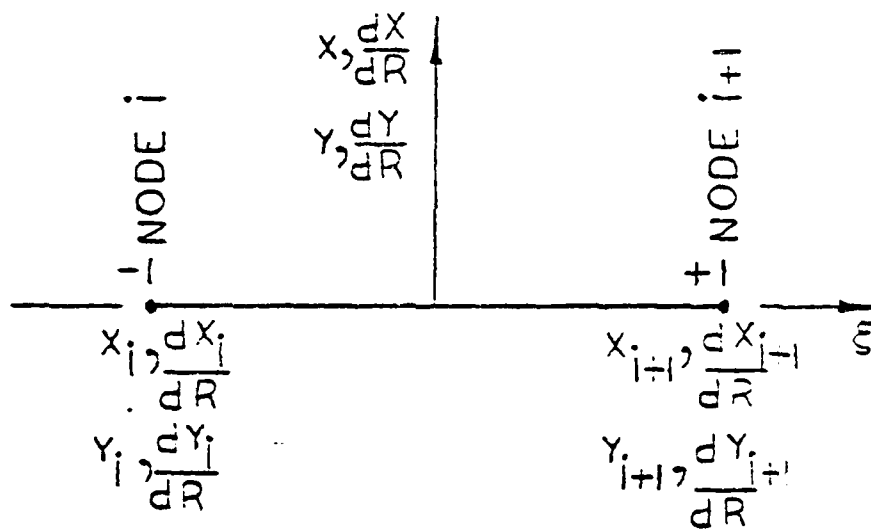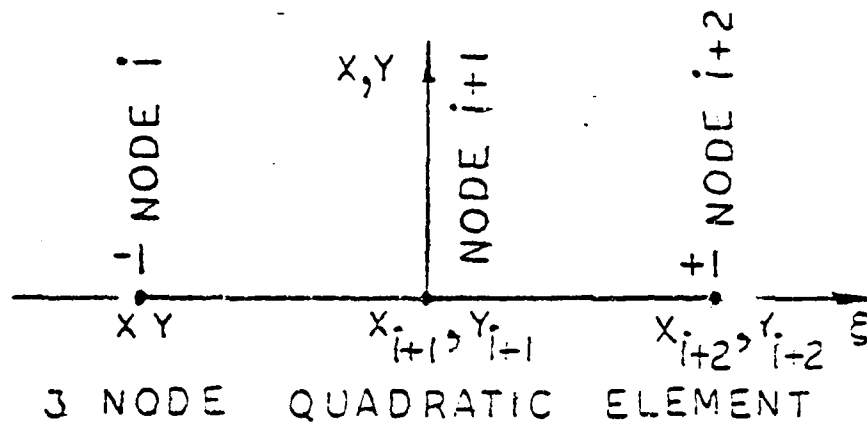
ξ = ELEMENT COORDINATE

R = GLOBAL COORDINATE

FIGURE 2.2   QUADRATIC AND CUBIC ELEMENTS

and $\{\psi(\xi)\} = \left\{ 0, \varphi_1(\xi), 0, \varphi_2(\xi), 0, \varphi_3(\xi) \right\}^T$

where $\varphi_1(\xi) = \frac{1}{2}\xi(\xi - 1)$

$\varphi_2(\xi) = 1 - \xi^2$

$\varphi_3(\xi) = \frac{1}{2}\xi(1 + \xi)$

The cubic two-node element nodal variables are

$$\{u\}_e^T = \left\{ X_i, \frac{\partial X_i}{\partial R}, Y_i, \frac{\partial Y_i}{\partial R}, X_{i+1}, \frac{\partial X_{i+1}}{\partial R}, Y_{i+1}, \frac{\partial Y_{i+1}}{\partial R} \right\}^T \qquad (2.4.3)$$

The associated interpolation functions on $(-1, 1)$ are

$$\{\varphi(\xi)\}^T = \left\{ \varphi_1(\xi), \varphi_2(\xi), 0, 0, \varphi_3(\xi), \varphi_4(\xi), 0, 0 \right\}^T \qquad (2.4.4)$$

and

$$\{\psi(\xi)\}^T = \left\{ 0, 0, \varphi_1(\xi), \varphi_2(\xi), 0, 0, \varphi_3(\xi), \varphi_4(\xi) \right\}^T$$

where $\quad \varphi_1(\xi) = \frac{1}{4}\left(2 - 3\xi + \xi^3\right)$

$$\varphi_2(\xi) = \frac{\Delta}{4}\left(1 - \xi\right)^2\left(1 + \xi\right)$$

$$\varphi_3(\xi) = \frac{1}{4}\left(1 + \xi\right)^2\left(2 - \xi\right)$$

$$\varphi_4(\xi) = \frac{\Delta}{4}\left(\xi - 1\right)\left(1 + \xi\right)^2$$

and $\quad \Delta = \quad \frac{1}{2} \quad$ the length of the element in the global

system.

2.5 . Boundary Conditions.

When stationary values of the integral functional given in

(1.2.1) are to be determined it is necessary to enforce the essential

boundary conditions which are determined using variational calculus.

The essential boundary conditions for (1.2.1) are

$$\frac{\partial F}{\partial u'} \, \delta u \;=\; 0 \qquad\qquad (2.5.1)$$

at the boundaries. If $\quad u \quad$ is not specified at a boundary then

$\frac{\partial F}{\partial u'} = 0 \quad$ there. In the finite element analysis this require-

ment determines a set of equations which the nodal variables must

satisfy. The requirement that the gradient, $\{g\}$, be zero still

applies. A gradient equation with a reduced dimension must then be

found. The new equation specifies the location of stationary values

of the discrete energy functional for which the nodal variables also

satisfy the boundary conditions.

The axisymmetric problems analyzed in this study are one dimen-

sional boundary value problems. The boundary conditions for such

problems specify relations among the nodal variables in only the first

and last elements. Then, the computation of the gradient and Hessian

is modified only for these boundary elements. Each boundary equation

is arranged to express the nodal variable at the boundary in terms of

the remaining, reduced, element nodal variables. When this has been

done we can determine the full set of nodal variables in terms of the

reduced nodal variables. We have

$$\{u\}_e = [C]_e \{u\}_{eR} \qquad (2.5.2)$$

where $\{u\}_{eR}$ = the reduced set of nodal variables

and $[C]_e$ = the matrix of coefficients determined by the

constraint.

With expression (2.5.2) computation of the reduced global gradient and

Hessian is easily accomplished. If we substitute (2.5.2) into (2.2.1) we arrive at

$$A(\xi, \{u\}_{eR}^T) = \{u\}_{eR}^T [C]_e^T \{\dot{\varphi}(\xi)\} = \{\dot{\varphi}(\xi)\}^T [C]_e \{u\}_{eR} = A(\xi, \{u\}_{eR})$$

$$(2.5.3)$$

$$B(\xi, \{u\}_{eR}^T) = \{u\}_{eR}^T [C]_e^T \{\dot{\psi}(\xi)\} = \{\dot{\psi}(\xi)\}^T [C]_e \{u\}_{eR} = B(\xi, \{u\}_{eR})$$

$$C(\xi, \{u\}_{eR}^T) = \{u\}_{eR}^T [C]_e^T \{\varphi(\xi)\} = \{\varphi(\xi)\}^T [C]_e \{u\}_{eR} = C(\xi, \{u\}_{eR})$$

The element gradient and Hessian will then have the same scalar coefficients as those given in (2.2.5) and (2.3.2). Only the vectors and matrices need to be modified and we arrive at

$$\{g\}_{eR} = [C]_e^T \{g\}_e$$

$$(2.5.4)$$

$$[k]_{eR} = [C]_e^T [k]_e [C]_e$$

CHAPTER 3

AXISYMMETRIC DEFORMATION OF A DISK
WITH A HOLE

3.1 Introduction.

In 1951 Rivlin and Thomas[12] studied the in-plane behavior of a
thin disk of Mooney material. The disk contained a central circular
hole and was radially loaded on its outer edge. Rivlin and Thomas'
analysis compared well with experimental test data. They determined
that a value of 0.1 for α in equation (1.1.5) leads to computa-
tional results that are in good agreement with experimental test data.
Using the cylindrical coordinate systems shown in Figure 3.1 Rivlin
and Thomas assumed that the sheet was thin enough so that the deforma-
tions are not dependent on Z. Further, they considered only axisym-
metric deformations, which eliminates dependence on Θ. The result
is that the axisymmetric deformation of a thin disk is a pure strain
deformation with the stretch ratios dependent on only R. They
obtained an approximate analytical solution to this finite deformation
problem as follows. Expressions for all the radial and tangential
stretch ratios λ_1 and λ_2 were determined in terms of the inde-
pendent coordinate ρ, the dependent coordinate R, and the form of
the internal energy W. These expressions were used with the
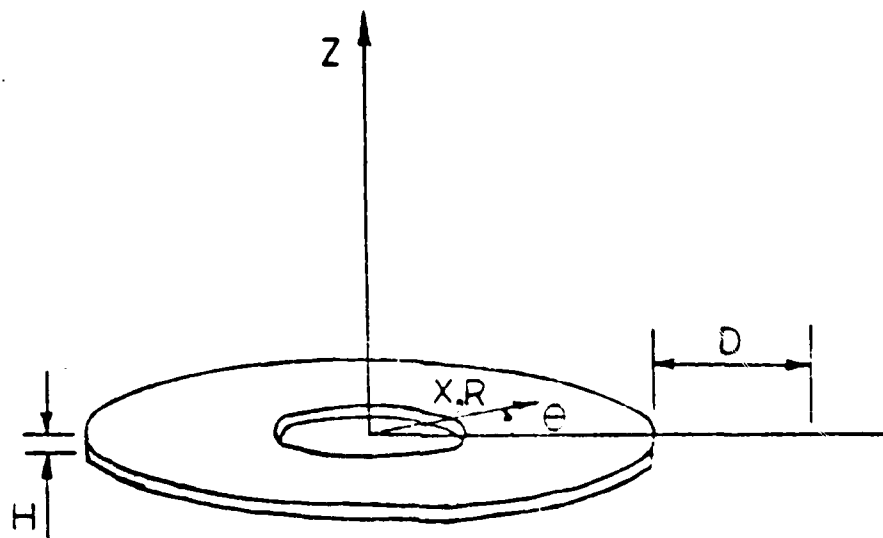
D = ENFORCED DISPLACEMENT OF OUTER EDGE

H = THICKNESS OF SHEET = 1.0

R = UNDEFORMED COORDINATES

X = DEFORMED COORDINATES

FIGURE 3.1   DISK WITH HOLE.

equilibrium equation and boundary conditions to determine the first

three coefficients of a Taylor expansion of the solution. The Taylor

expansion being

$$\rho(R) = \sum_{N=0}^{\infty} \frac{1}{N!} (R-A)^N \left(\frac{d^N \rho}{dR^N} \right) \Bigg|_{R=A} \tag{3.1.1}$$

where $A =$ the internal radius of the disk.

A numerical solution to this problem was found by assuming knowledge of

λ_1 and λ_2 at a particular radius $R = R^1$. The equilibrium

equation and a differential equation obtained by eliminating the inde-

pendent variable ρ from the expressions for λ_1 and λ_2

were used with the incompressibility condition $\lambda_1 \lambda_2 \lambda_3 = 1$

to obtain approximate expressions for λ_1 and λ_2 at nearby

values of R and thus for all values of R.

Recently Verma and Rana[13] considered the axisymmetric in-plane

deformation of a disk with a hole. They used a strain energy function

which is different than the Mooney form. The energy function used is

$$W = \frac{2G}{N} I_E + B I_E^M \tag{3.1.2}$$

where $\qquad \mathbb{I}_E \;=\; \dfrac{\lambda_1^N + \lambda_2^N + \lambda_3^N - 3}{N}$

and $\qquad G, B \;=\;$ material constants.

When $\quad N = 1 \quad$ and $\quad M = 1 \quad$ (3.1.2) reduces to (1.1.5) with

$\alpha = 0.0 \quad$. Under these conditions on N and M Verma

and Rana reduce their general equation to a special equation called the

Varga equation. They compare the solution of this equation to both

Rivlin and Thomas' three-term Taylor expansion of the solution for

Mooney material and experimental data. The three-term expansion com-

pared better with experimental data. This may be because using

$N = 1 \quad$ and $\quad M = 1 \quad$ in (3.1.2) implies a slightly different

form of the strain energy than the Mooney form. In the Mooney form

the value of α was chosen to make the computed and measured data

agree well.

Finite element solutions to the axisymmetric deformation of an

incompressible disk with a hole have been obtained by a different

finite element technique than presented in this study. In 1967

Oden[14] presented a method for obtaining numerical solutions to prob-

lems in the theory of nonlinear elasticity. He used the finite element

method to formulate the nonlinear problem and solve it. Most of the
finite element formulations used previous to that of Oden were based
on finding successive corrections to the linear problem. Oden discret-
ized the domain of the elastic body into subdomains called finite
elements. The discretization was assumed fine enough so that the dis-
placements vary linearly within an element. The expressions describing
the linear interpolation of the displacements inside an element in
terms of the nodal displacements were used to obtain expressions for
the strains in an element. These strain expressions are used with the
nonlinear theory of elasticity to obtain the strain energy in an
element in terms of the nodal displacements. Expressions for the
generalized forces acting on an element are derived and the total
potential energy for the finite element is computed. The condition of
minimum potential energy is used to determine a set of nonlinear equi-
librium equations for the element. A global coordinate system is used
and the appropriate transformations are applied so that the element
equilibrium equations are expressed in the global system. The
assembled global nonlinear equations are then determined and solved.
A solution of the disk problem analyzed in this chapter by Oden's
method is given in reference 4, chapter IV.

3.2 Analysis of a Disk with a Hole.

In this section we analyze the disk problem stated in section 3.1.
The disk has an inner radius of 1.0 and an outer radius of 3.0. The
boundary conditions are an enforced displacement of the outer edge and
a stress-free inner edge. The finite element method outlined in chapter 2 is used. The thickness of the disk and the material constant C_1
in (1.1.5) will both be unity. The outer edge of the disk will be
given a prescribed displacement and an initial guess of the solution
will be used to start the Newton algorithm. The quadratic three-node
element will be used with two and four point Gauss-Legendre integration.

Referring to Figure 3.1 the radial stretch ratio, λ_1, and
the tangential stretch ratio, λ_2, can be computed. They are

$$\lambda_1 = \frac{dx}{dR}$$

(3.2.1)

and
$$\lambda_2 = \frac{x}{R}$$

Using the incompressibility condition (1.1.2) the third stretch ratio
is

$$\lambda_3 = \frac{R}{X \frac{dX}{dR}} \qquad (3.2.2)$$

The radius, R, is the only independent variable and X is the only

dependent variable. Partition the domain of R into a uniform mesh for

quadratic three-node elements each of length $2(\Delta R)$. Each

element is mapped to ξ coordinates belonging to the interval

(-1, 1) by the mapping function

$$R = R_c + \Delta \xi \qquad (3.2.3)$$

where R_c = the radial displacement to the center node of

the undeformed element.

These relations were used in the finite element analysis described in

chapter 2 to compute the numerical data described in this chapter. To

start the Newton algorithm all nodes were moved radially outward by

the amount the outer edge was being displaced. With no nodal force

associated with the innermost node the traction-free boundary con-

dition at the inner radius is satisfied. The outermost element's nodal

displacements must be reduced in number because of the enforced displacement at the outer edge. If the enforced displacement of the outermost node is defined in the initial guess then the outermost element's gradient and Hessian can be modified as follows and the enforced displacement boundary condition will be satisfied.

$$\{g\}_{NR} = \left[C \right]_N^T \{g\}_N \qquad (3.2.4)$$

and

$$\left[k \right]_{NR} = \left[C \right]_N^T \left[k \right]_N \left[C \right]_N$$

where $N = $ the outermost element's identification number

and

$$\left[C \right]_N = \begin{bmatrix} 1 & 0 & 0 \\ 0 & 1 & 0 \end{bmatrix}$$

The finite element program used to obtain the data for this problem was written in double precision. The Newton algorithm was terminated when the ℓ_2 norm of the gradient was less than 10^{-8}. The ℓ_2 norm of the displacement increments was less than 10^{-10}

when the algorithm was terminated indicating that the displacement vector had converged in the Newton algorithm to more than eight significant digits.

The data presented by Rivlin and Thomas in reference 12 was used to define four problems. The stretch ratios, λ_2, at R = 3.0 were read from the four curves on the graph of λ_2 vs R in reference 12. These values of λ_2 were used to determine four values for the outer edge displacement, D, of the disk shown in Figure 3.1. The curves of λ_2 vs R which result from the finite element analyses are shown in Figure 3.2. The changes of λ_2 vs R with mesh size and integration order are not detectable graphically and these differences are discussed in the next section. The agreement between Rivlin and Thomas' computations and the finite element computations for λ_2 is good. The distribution of the strain invariants I_1 and I_2 as predicted by the finite element analyses is shown in Figures 3.3 and 3.4. These curves also agree well with the data presented in reference 12.

3.3 Convergence of the Finite Element Solutions.

To study the convergence rate of the displacement approximations the rate of convergence of the inner radius of the disk with respect to
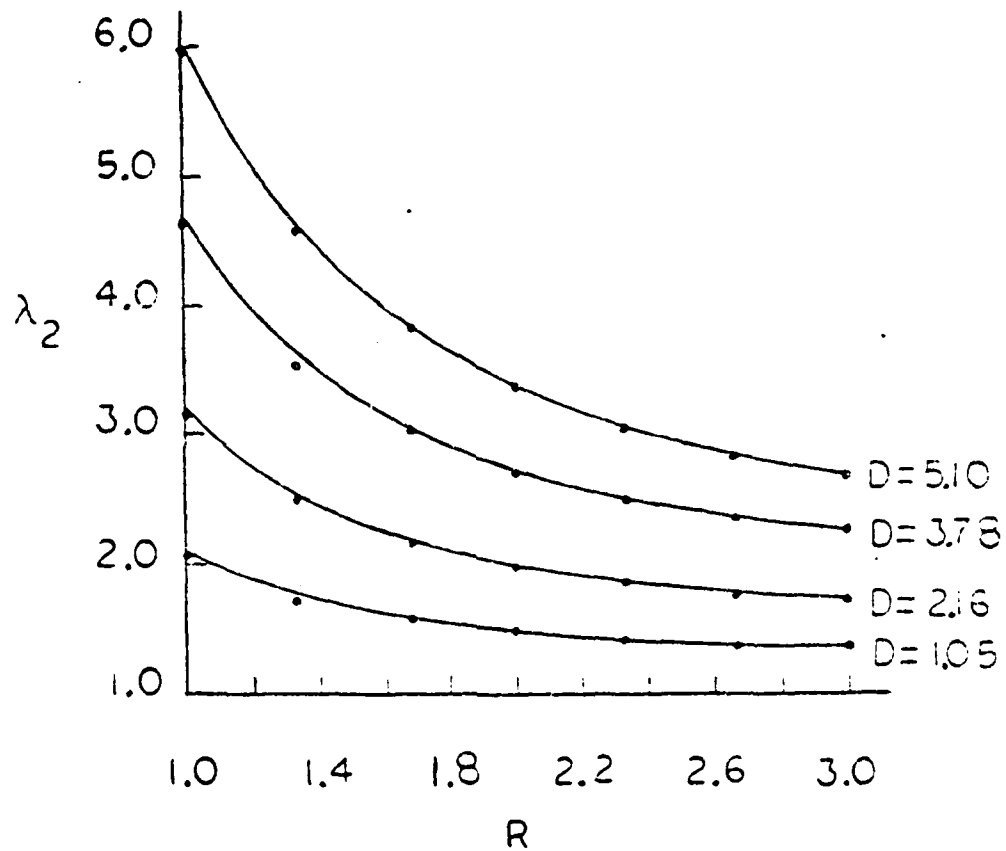
FIGURE 3.2 λ_2 VS R   FOR DISK
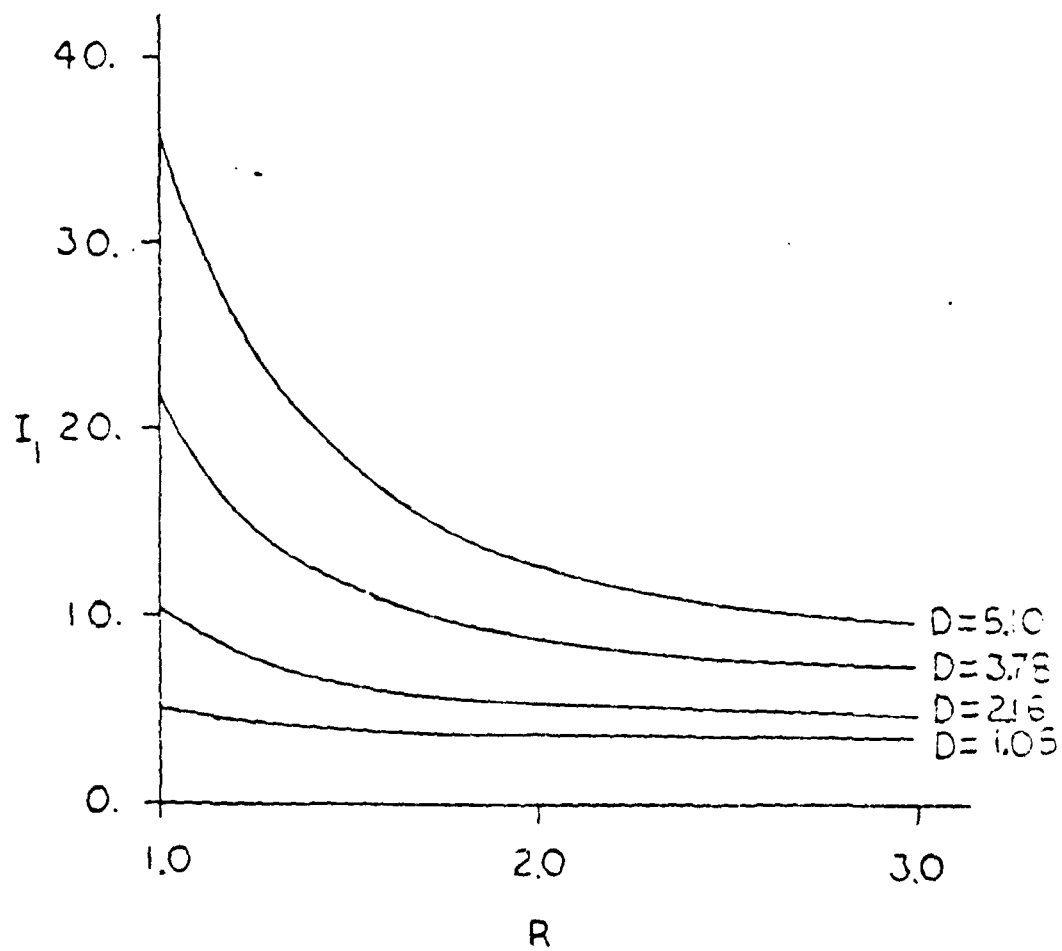WITH HOLE

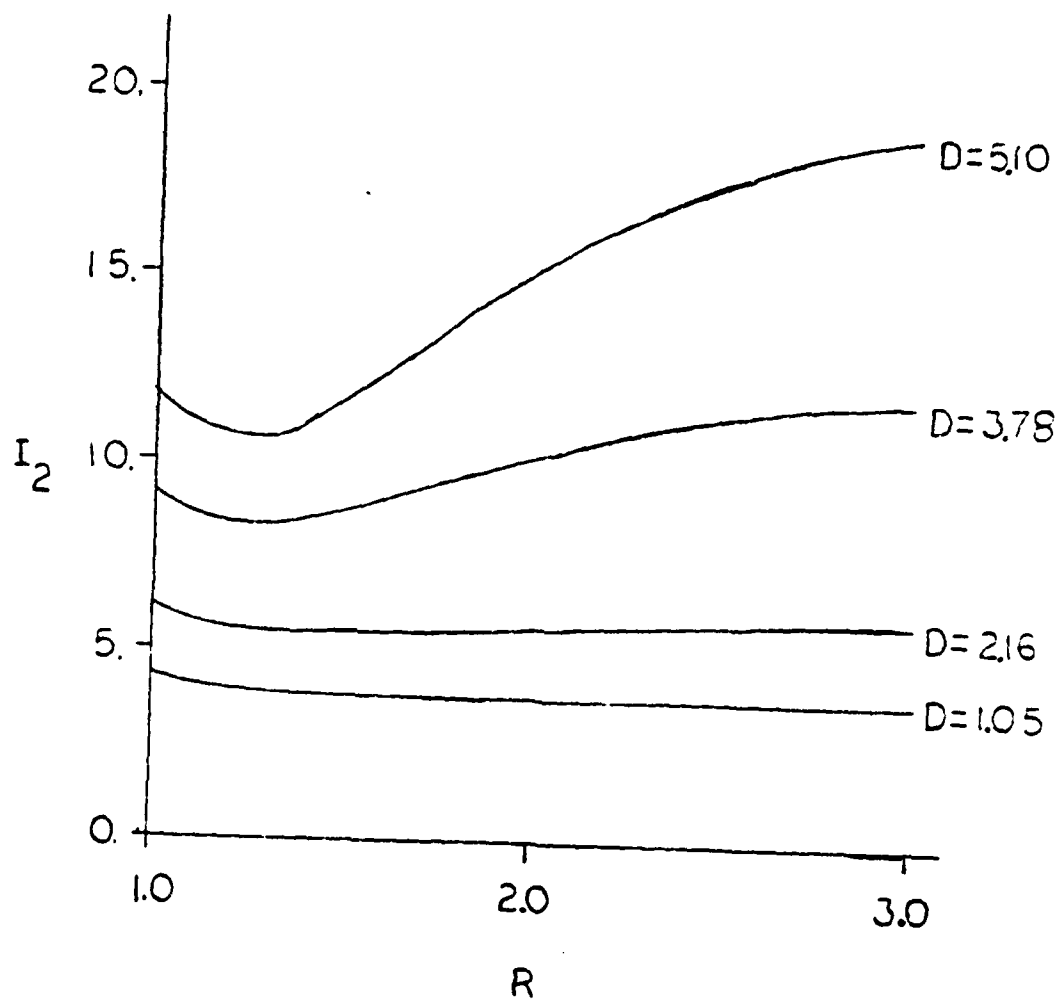FIGURE 3.3 I_1 VS R FOR DISK WITH
                HOLE

FIGURE 3.4 I_2 VS R FOR DISK WITH HOLE

a uniform mesh refinement was determined. We assume that we have the following power form of convergence.

$$\widehat{u}_N - u \doteq c \, H_N^P \qquad (3.3.1)$$

where $\widehat{u}_N$ = the finite element inner radius for N elements

u = the converged finite element inner radius

H_N = the element size for N elements

P = the convergence rate

C = a constant which is not dependent on the mesh size.

When (3.3.1) is used with the data in Table 3.1 the convergence rate, P , and the converged displacement, u , can be determined for each integration order. The converged inner radius for two-point integration was equal to the converged inner radius for four-point integration to seven digits (see Table 3.1). The rank of the element Hessians was determined in the first and last iterations. They were full rank in both cases. Also, the converged solution had a positive definite Hessian. Figure 3.5 shows the convergence rates and accuracy

TABLE 3.1 Convergence Data for Disk with Hole

Inner Radius (D = 5.10)

No. of Integration Points	6 Elements	9 Elements	12 Elements	Converged
2	5.9543663	5.9543443	5.9543404	5.9543385
4	5.9543421	5.9543393	5.9543388	5.9543386

Strain Energy (D = 5.10)

No. of Integration Points	6 Elements	9 Elements	12 Elements	Converged
2	302.08010	302.08307	302.08359	302.08384
4	302.08415	302.08390	302.08385	302.08382
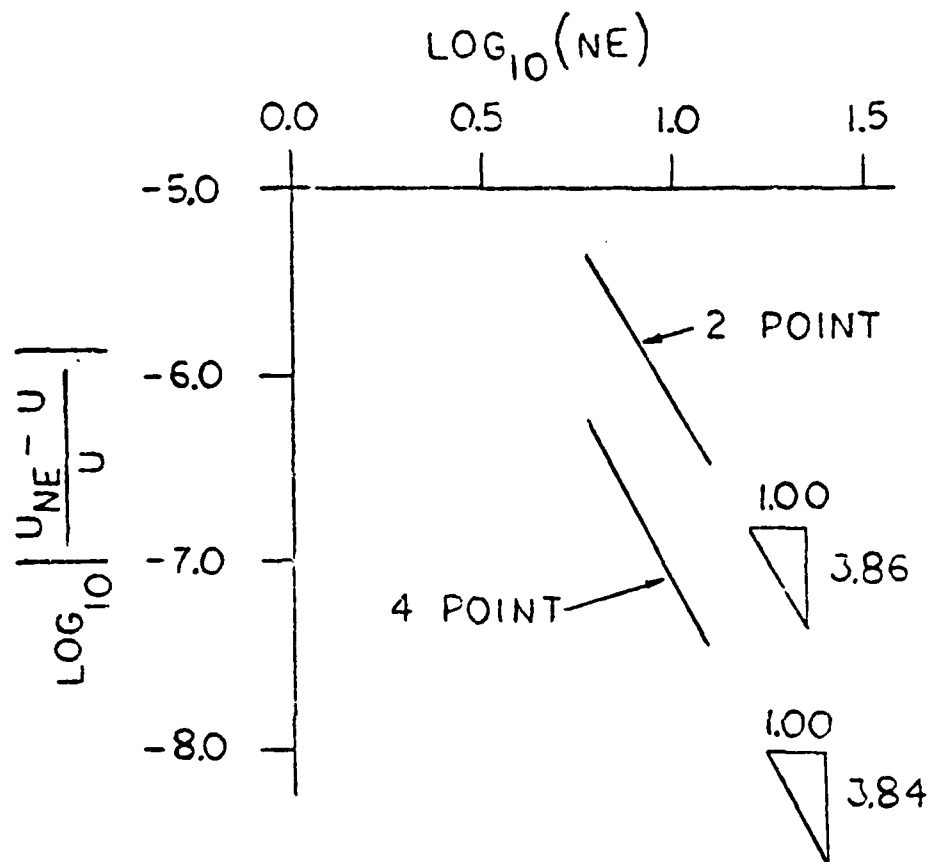
FIGURE 3.5 CONVERGENCE OF INNER
RADIUS-DISK WITH HOLE

of the finite element solutions associated with using both two-point and four-point integration for computing the element matrices. The convergence rates are nearly identical but four-point integration gave better accuracy by a full order of magnitude.

The convergence rate of the energy approximations was determined by the same method that was used to compute the convergence rate for the displacement approximations. Figure 3.6 shows that the convergence rate using two-point integration was only slightly greater than the convergence rate associated with four-point integration. However, the accuracy of the energy approximations associated with four-point integration was an order of magnitude better than the accuracy associated with two-point integration.
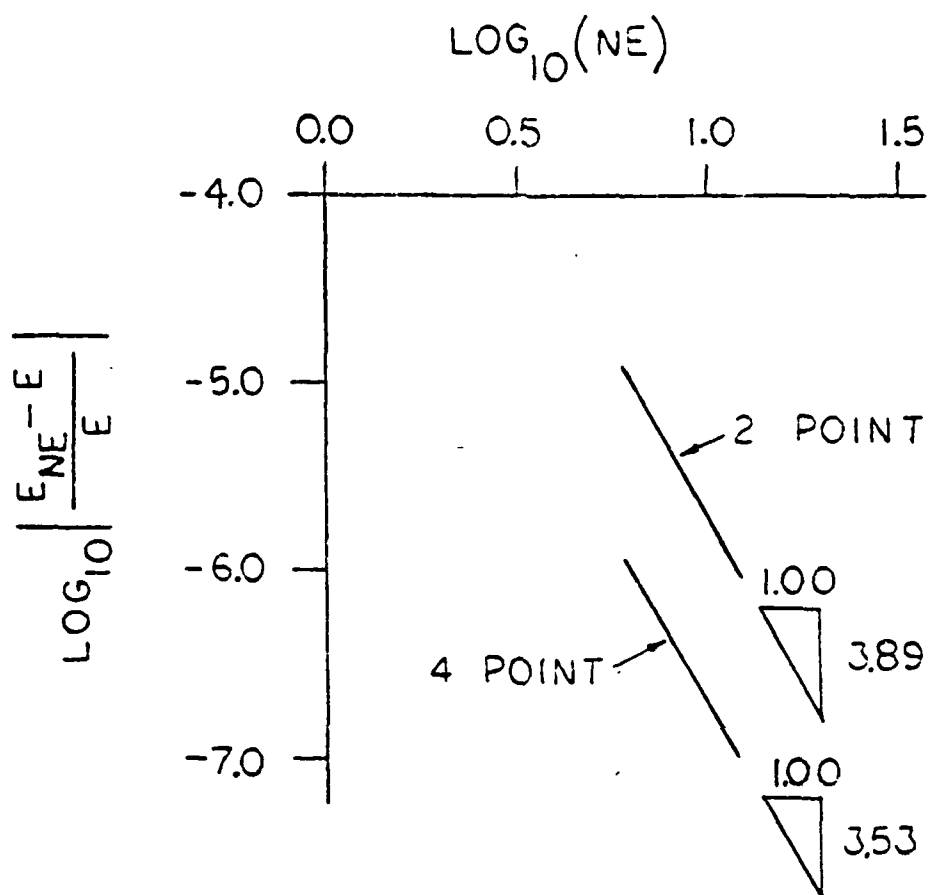
FIGURE 3.6   CONVERGENCE OF STRAIN
ENERGY—DISK WITH HOLE

CHAPTER 4

INFLATION OF A CIRCULAR DISK

4.1 Introduction.

The inflation of an initially flat circular disk, see Figure 4.1, made of incompressible material was analyzed by Adkins and Rivlin[15] and Green and Adkins[16]. It is assumed that the deformed disk has principal radii of curvature that are everywhere large compared with the thickness of the disk. This allows the stress variation over the thickness of the disk to be neglected in the analysis. Adkins and Rivlin used the six differential equations derived by Love[17] to represent the equilibrium of a thin sheet. Four of these equations are identially satisfied when the symmetry conditions are introduced leaving only two equations to be solved. The two principal tractions are the dependent variables, and the deformed radius is the independent variable. Expressions for these tractions are derived in terms of the stretch ratios and the strain energy function. The stretch ratios are then determined in terms of the undeformed and deformed coordinates. An approximate solution is then found by a technique similar to the technique used to find the approximate solutions for the disk with a hole mentioned in Chapter 3.
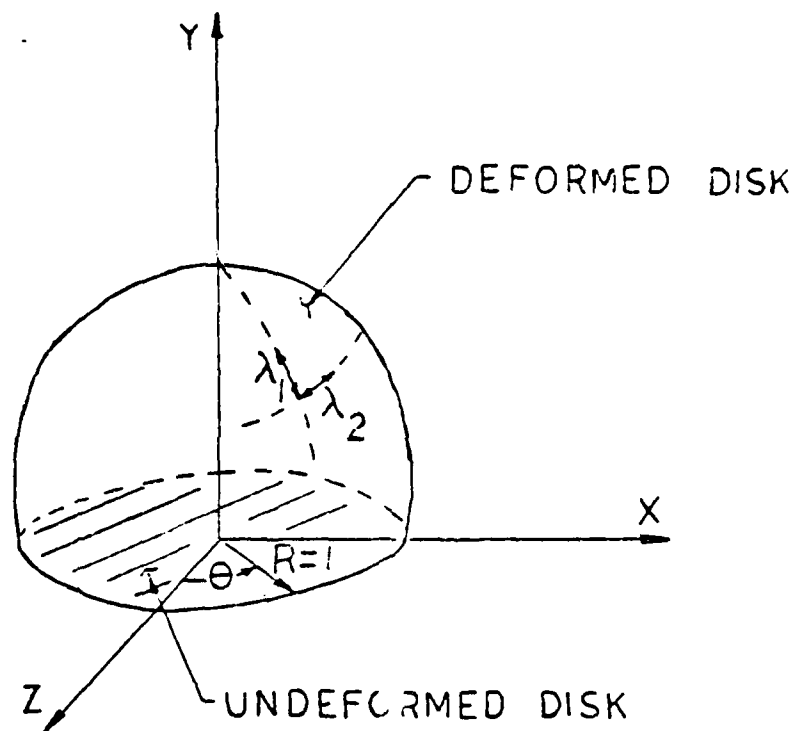
FIGURE 4.1   INFLATION OF CIRCULAR
DISK.

A different analysis of the axisymmetric deformations of nonlinear membranes was made by Yang and Feng[18] in 1970. In their paper the stretch ratios λ_1 and λ_2 in the meridian and circumferential directions respectively are parametrically expressed in terms of coordinates $\rho(R)$ and $\eta(R)$, and a function $\beta(\rho)$ which specifies the undeformed configuration. The parametric variable R is the radial coordinate from the axis of symmetry. The equilibrium equations of an axisymmetric membrane loaded with an internal pressure and a constitutive equation expressing the relationship between the principal tractions and stretch ratios are used. Three new functional variables u, ν, and w are defined in terms of ρ, η, $\frac{d\rho}{dR}$, and $\frac{d\eta}{dR}$ so that the equations of equilibrium reduce to a set of first order ordinary differential equations. In the analysis of the inflation of a circular disk they are able to reduce the problem to a nondimensional form which allows the solutions to be obtained if a stretch ratio at the pole is assumed. That is, if a stretch ratio at the pole is assumed then a configuration and pressure is determined which produces the assumed stretch ratio at the pole. Their results · compared well with the earlier work of Adkins and Rivlin[15]. Tielking and Feng[7] used the potential energy principle and the Ritz method in 1974 to determine the deformation profiles of an inflated disk and their

results compare well with Yang and Feng's work.

The finite inflation of a circular disk has been analyzed by the finite element method. In reference 4 Oden gives a summary of the work done from 1966 to 1971. In Oden's analysis the displacement interpolation was linear and the strain energy function involved the strain invariants in an exponential form. The exponential form of the strain energy used approximates the Mooney form for the material constants used in the analysis. The results of the finite element analysis were compared with experimental data and the agreement was good. Oden noted the highly nonlinear character of this problem by presenting a graph of the inflation pressure vs the polar extension ratio. Certain values of pressure have more than one associated polar extension ratio indicating that the deformation is not uniquely defined in terms of the polar extension ratio. Recently Argyris et al[19] considered the use of higher order elements for the analysis of the finite inflation of a circular disk made of Mooney material. The data obtained using higher order elements, quadratic interpolation, was compared to data obtained using linear interpolation. The results indicated that the use of quadratic interpolation elements leads to better accuracy with fewer elements.

4.2 Analysis of the Inflation of a Circular Disk.

The inflation of an initially flat circular disk of unit radius is analyzed here. The Mooney form of the energy is assumed with

$$C_i = 1.0 \quad \text{and} \quad \alpha \approx 0.1 \quad \text{in equation (1.1.5). Due to the}$$

symmetry involved only the radial domain (o, 1) has to be discretized. The boundary conditions are zero displacement at the outer edge and zero slope at the pole. The incremental pressure-formulation is used. The solution algorithm was started with an initial out-of-plane deformation. The quadratic three-node element is used with two- and four-point Gauss-Legendre integration.

We use X as the radial displacement and Y as the vertical displacement of the points along the radius of the undeformed disk, see Figure 4.1. Then, the meridional stretch ratio, λ_1, and the circumferential stretch ratio, λ_2, can be computed. They are

$$\lambda_1 = \left(\left(\frac{dX}{dR} \right)^2 + \left(\frac{dY}{dR} \right)^2 \right)^{1/2} \tag{4.2.1}$$

and

$$\lambda_2 = \frac{X}{R}$$

The incompressibility condition $\lambda_1 \lambda_2 \lambda_3 = 1$ yields the third stretch ratio

$$\lambda_3 = \frac{R}{X \left(\left(\frac{dX}{dR}\right)^2 + \left(\frac{dY}{dR}\right)^2 \right)^{1/2}} \qquad (4.2.2)$$

The radius, R, is the only independent variable. X and Y are the functions of R to be approximated. The domain of R is partitioned for a uniform mesh of quadratic three-node elements as in chapter 3. The mapping function (3.2.3) is used and the finite element solutions are determined by the method described in chapter 2. The constraint equations which represent the boundary condition at the pole, $R = 0$, can be computed with the aid of Figure 4.2. In element coordinates we have

$$Y(\xi) = \left\{ \Psi(\xi) \right\}^T \left\{ u \right\}_1 \qquad (4.2.3)$$

then $\quad Y(\xi) = \frac{1}{2}\xi(\xi-1)Y_1 + (1-\xi^2)Y_2 + \frac{1}{2}\xi(\xi+1) \qquad (4.2.4)$
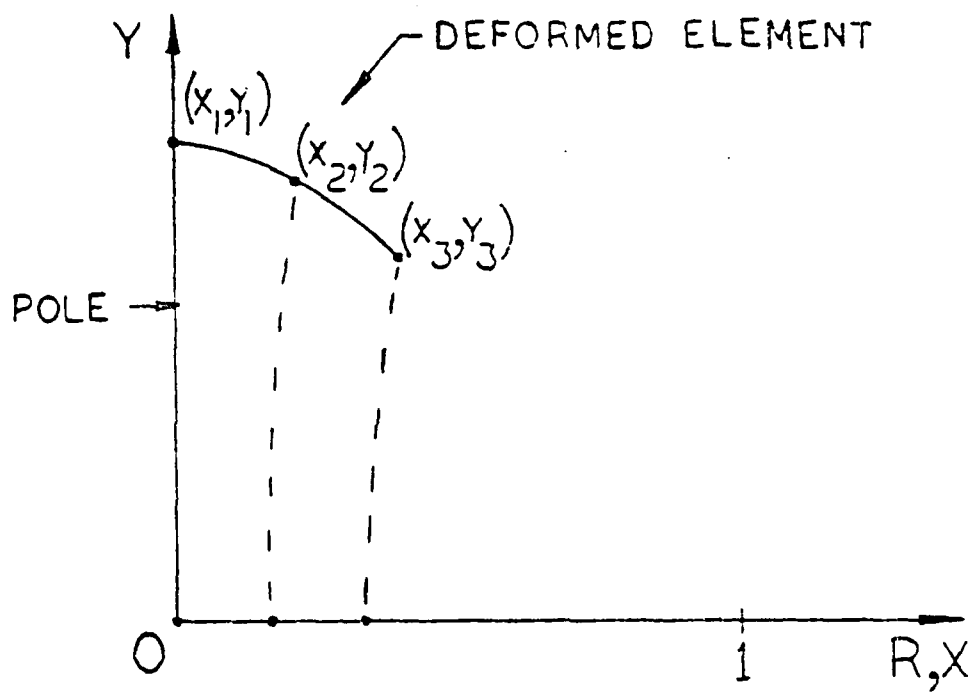
FIGURE 4.2   ELEMENT AT POLE - IN-

FLATION OF DISK.

we require
$$\left.\frac{dY}{d\xi}\right|_{\xi=-1} = 0 \tag{4.2.5}$$

and
$$X\Big|_{\xi=-1} = 0$$

Using (4.2.4) and (4.2.5) we obtain

$$
\begin{Bmatrix} X_1 \\ Y_1 \\ X_2 \\ Y_2 \\ X_3 \\ Y_3 \end{Bmatrix} =
\begin{bmatrix}
0 & 0 & 0 & 0 \\
0 & \frac{4}{3} & 0 & -\frac{1}{3} \\
1 & 0 & 0 & 0 \\
0 & 1 & 0 & 0 \\
0 & 0 & 1 & 0 \\
0 & 0 & 0 & 1
\end{bmatrix}
\begin{Bmatrix} X_2 \\ Y_2 \\ X_3 \\ Y_3 \end{Bmatrix}
\tag{4.2.6}
$$

or $\{u\}_1 = [C]_1 \{u\}_{1R}$ \hfill (4.2.7)

The constraint relation for the element at the outer edge of the disk is

$$
\begin{Bmatrix} X_{N-2} \\ Y_{N-2} \\ X_{N-1} \\ Y_{N-1} \\ X_N \\ Y_N \end{Bmatrix} = \begin{bmatrix} 1 & 0 & 0 & 0 \\ 0 & 1 & 0 & 0 \\ 0 & 0 & 1 & C \\ 0 & 0 & 0 & 1 \\ 0 & 0 & 0 & 0 \\ 0 & 0 & 0 & 0 \end{bmatrix} \begin{Bmatrix} X_{N-2} \\ Y_{N-2} \\ X_{N-1} \\ Y_{N-1} \end{Bmatrix}
\tag{4.2.8}
$$

$$
\text{or} \quad \{u\}_{Ne} = \begin{bmatrix} C \end{bmatrix}_{Ne} \{u\}_{Ne\,R}
\tag{4.2.9}
$$

The first and last element gradients and Hessians are modified with the constraint matrices of (4.2.9) and (4.2.7) by using (2.5.4).

The work, $\cdot W_e$, done by the pressure, P , acting on an element, (e) , during the deformation is

$$
W_e = \int\limits_{(e)} P \pi X^2 \, dY
$$

$$
\text{or} \quad W_e = -\pi P \int\limits_{(e)} X^2 Y' \, dR
\tag{4.2.10}
$$

The discrete form of (4.2.10) in element coordinates with p integration points is given as follows.

$$W_e = -\pi P \sum_{i=1}^{P} \omega_i \, C_i^2 \, B_i \qquad (4.2.11)$$

where C and B are given in (2.2.1).

The element gradient and Hessian work expressions calculated from (4.2.11) are

$$\frac{\partial W_e}{\partial \{u\}_e^T} = -\pi P \sum_{i=1}^{P} \omega_i \left(2 B_i C_i \{\varphi_i\} + C_i^2 \{\dot{\psi}_i\} \right) \qquad (4.2.12)$$

and

$$\frac{\partial^2 W_e}{\partial \{u\}_e \partial \{u\}_e^T} = -2\pi P \sum_{i=1}^{P} \omega_i \left(C_i \left[\{\varphi_i\}\{\dot{\psi}_i\}^T - \{\psi_i\}\{\varphi_i\}^T \right] + B_i \left[\{\varphi_i\}\{\psi_i\}^T \right] \right)$$

The stretch ratios λ_1 and λ_2 evaluated at the pole are equal since the circumferential stretch ratio becomes a meridional stretch ratio at that point. The stretch ratio λ_2 at the pole can not be computed directly from (4.2.1) and the nodal displacement data

since the radius R is zero there. In element coordinates we have

$$\lambda_{2\,pole} = \lim_{\xi \to -1} \left(\frac{1-\xi^2}{R_c + \Delta\xi} X_2 + \frac{\frac{1}{2}\xi(1+\xi)}{R_c + \Delta\xi} X_2 \right)$$

for the element at the pole. The stretch ratio, λ_2, at the pole then becomes

$$\lambda_{2\,pole} = \frac{2}{\Delta} X_2 - \frac{1}{2\Delta} X_3 \qquad (4.2.13)$$

Equations (4.2.1) to (4.2.13) were used in the finite element analysis described in chapter 2 to compute deformations of the inflated disk. The computer program was written in double precision. Cross-sectional profiles of the disk at three pressures are shown in Figure 4.3. These profiles were drawn using displacement data associated with 9 elements. The resulting stretch ratios for the same pressures are shown in Figures 4.4 and 4.5. The stretch ratios were drawn from data computed using 3 elements. Nodal data was graphed and a smooth curve fit to the nodal data over each element. The stretch ratios associated with 9 elements at $P = 5.50$ are also shown to graphically present
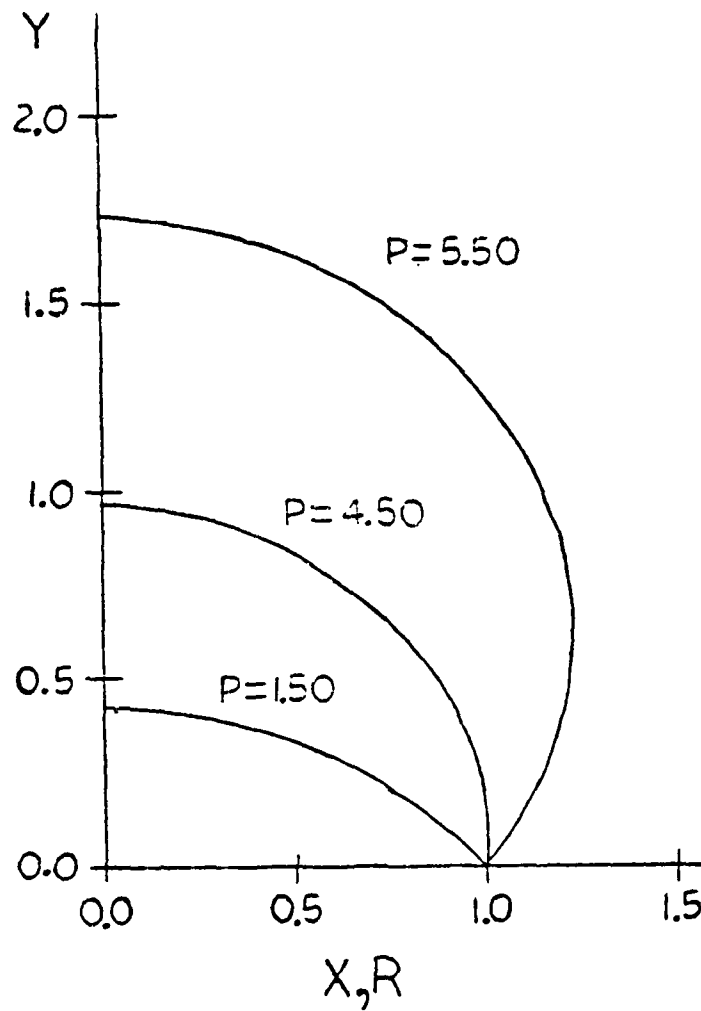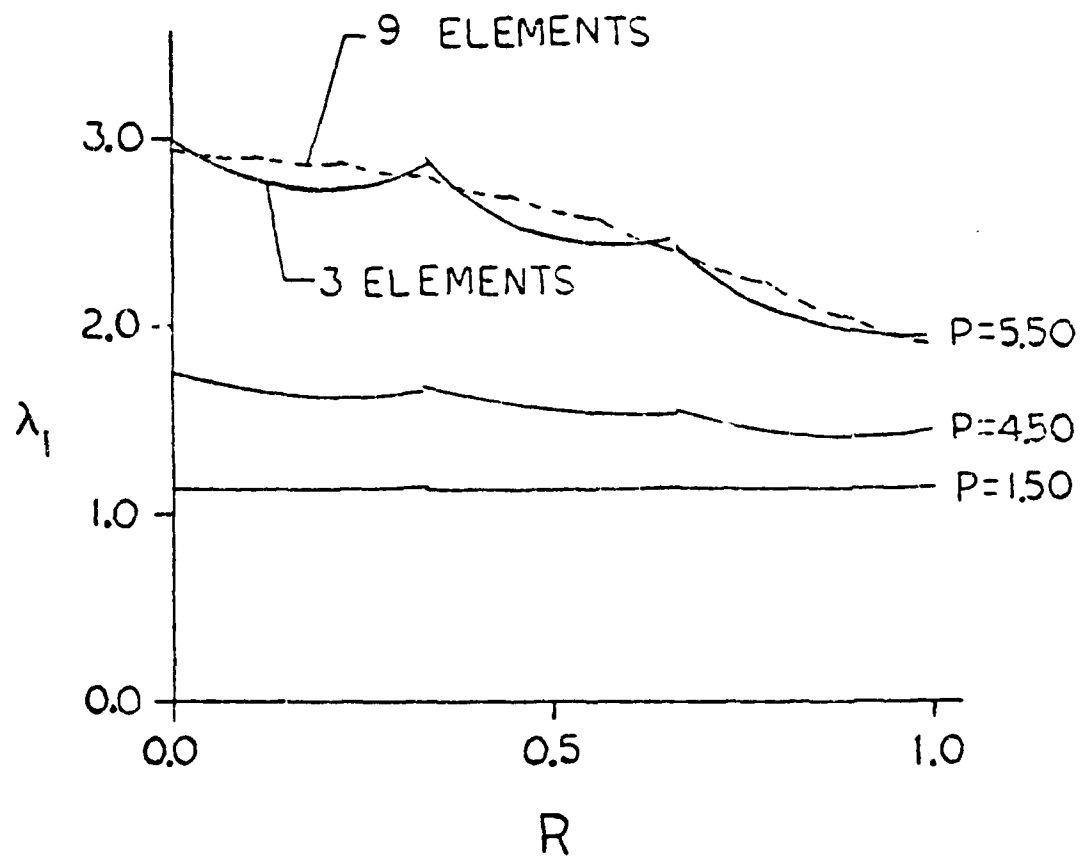
FIGURE 4.3   PROFILES OF INFLATED
DISK.

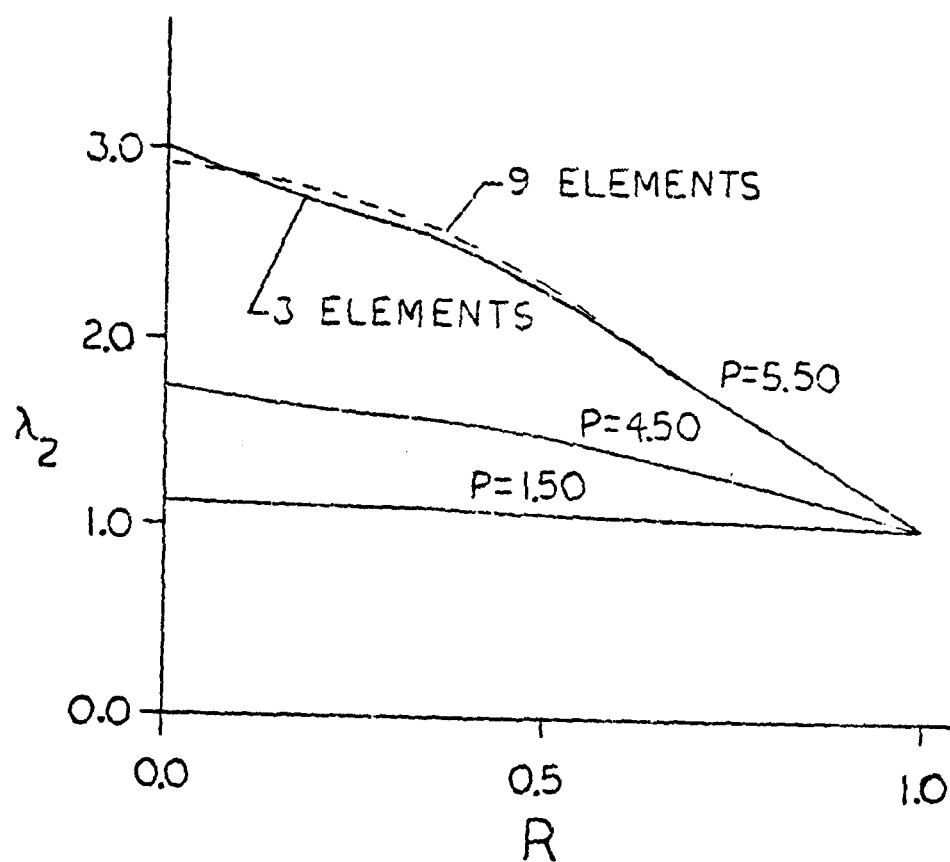FIGURE 4.4 λ_1 VS R FOR IN-
FLATED DISK.

FIGURE 4.5 λ_2 VS R FOR INFLATED DISK.

the changes computed in the stretch ratios as a result of mesh refine-
ment. The figures indicate that a mesh near 9 elements yields an
accuracy sufficient for most applications. Also, it appears that for a
coarse mesh the accuracy is best near the first and last nodes of these
three-node one-dimensional elements. The distributions of the strain
invariants for $\underline{P} = 5.50$ are shown in Figure 4.6.

4.3 Convergence of the Finite Element Solutions.

The rate of convergence of the displacement and energy approxima-
tions with respect to a uniform mesh refinement was determined by the
same method used in section 3.3. The computed pole displacement and
total strain energy values at a pressure $\underline{P} = 5.50$ and at
several mesh values are shown in Table 4.1. The computer program
written to obtain the data in Table 4.1 was written in double precision.
The computed converged data for two- and four-point integration in Table
4.1 compares well to six significant digits for the pole displacement
and to five significant digits for the strain energy. The pole dis-
placement is not a finite element approximation variable but is a
linear combination of two approximation variables through equation
(4.2.5). The results of the convergence calculations are displayed in
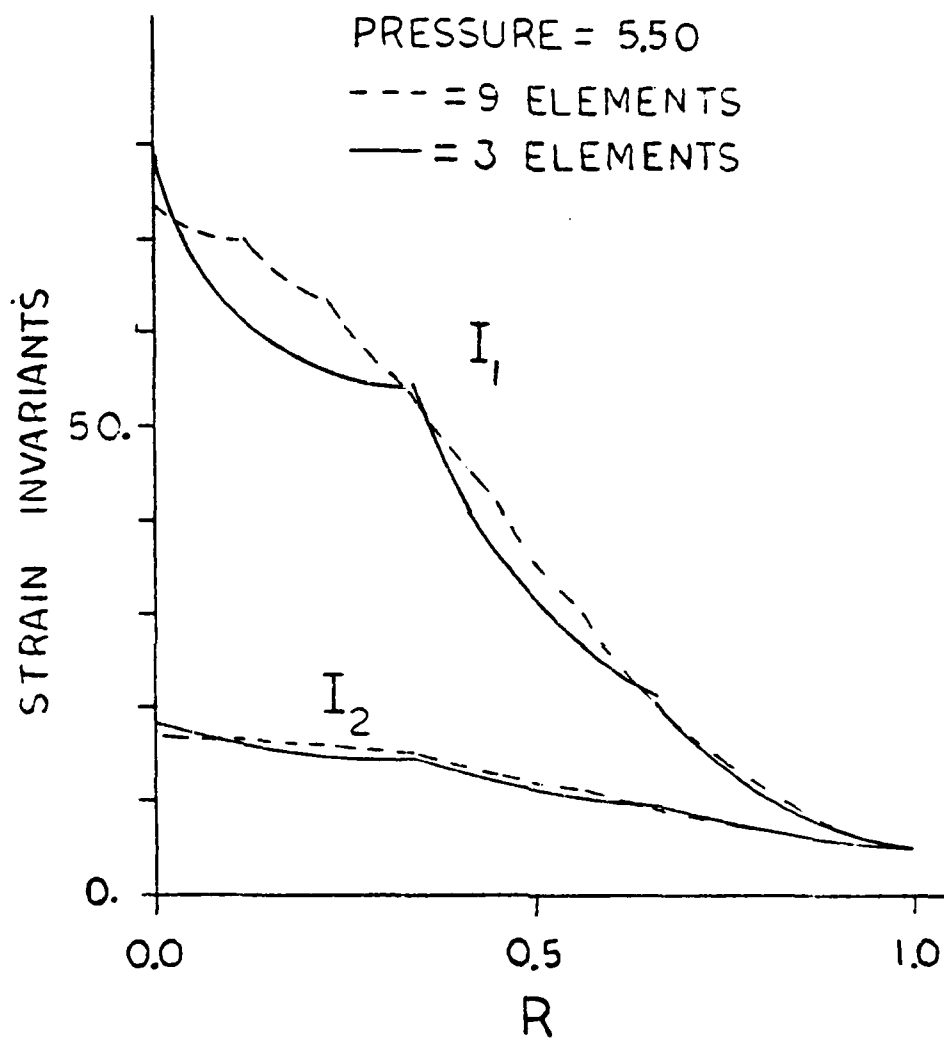Figures 4.7 and 4.8. The higher order integration was not helpful in

FIGURE 4.6   STRAIN   INVARIANTS VS
R FOR INFLATED DISK.

TABLE 4.1   Convergence Data for Inflation of Disk

Pole Displacement (P = 5.50)

No. of Integration Points	3 Elements	6 Elements	9 Elements	Converged
2	1.7012760	1.7331020	1.7350315	1.7355636
4	1.6862435	1.7321128	1.7348283	1.7355563

Strain Energy (P = 5.50)

No. of Integration Points	3 Elements	6 Elements	9 Elements	Converged
2	26.278508	26.402439	26.408690	26.410114
4	24.786216	26.301468	26.388629	26.411067
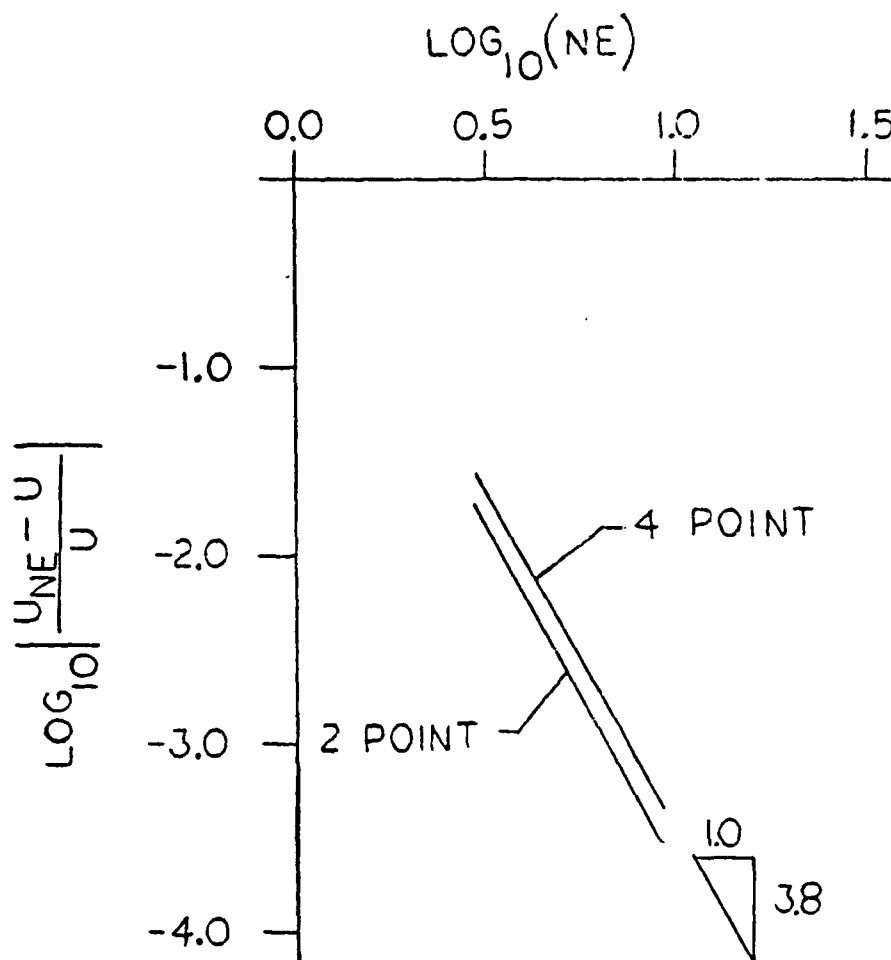
FIGURE 4.7   CONVERGENCE OF POLE
            DISPLACEMENT - INFLATED
            DISK.
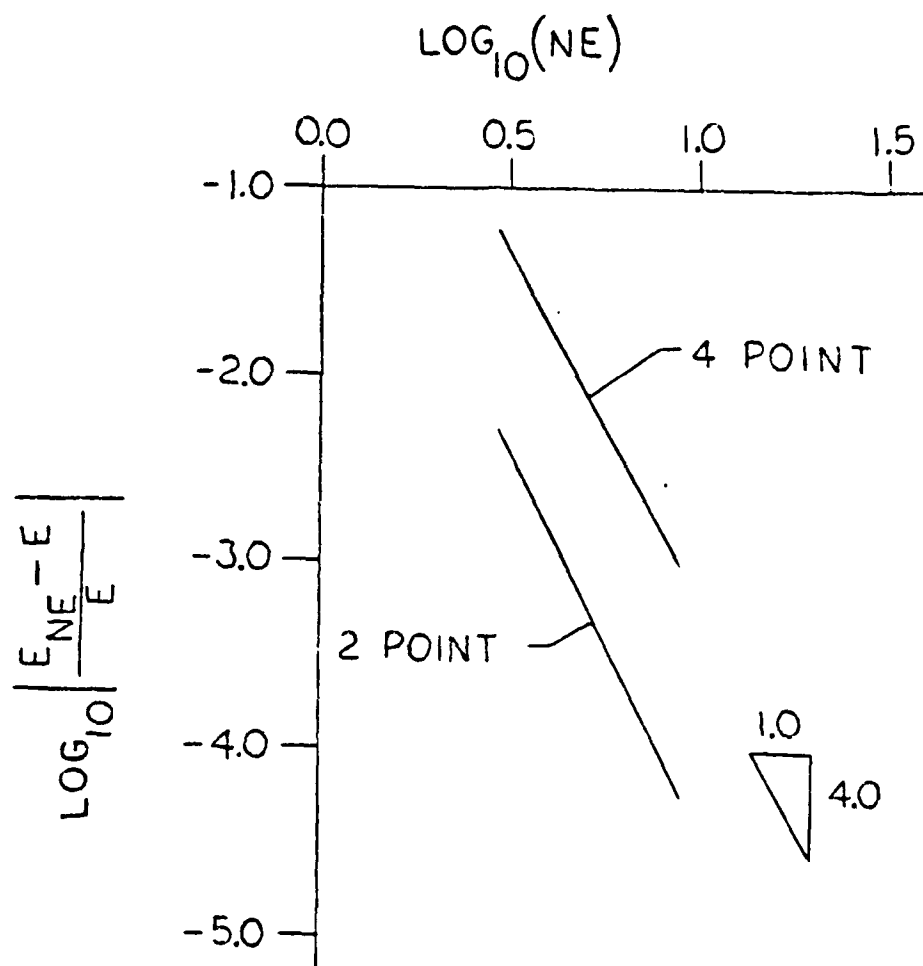
FIGURE 4.8   CONVERGENCE OF STRAIN
ENERGY - INFLATED DISK.

improving the accuracy of the computed displacement field and in fact

gave slightly less accurate results. The same results apply to the

accuracy of the strain energy. However, the two-point integration

scheme was an order of magnitude more accurate than the four-point

integration scheme for computation of the total strain energy.

4.4 Out-of-Plane Deformation of a Unit Disk with a Concentric

Rigid Inclusion.

The in-plane axisymmetric deformations of a rubber sheet with a

circular rigid inclusion has been investigated by Yang[19a] in 1967

and again by Verma and Rana[13] in 1978. The out-of-plane deforma-

tions due to a vertical axial force on the rigid inclusion and a

pressure on the membrane were determined in 1974 by Tielking and

Feng[7]. In this section the out-of-plane deformations resulting

from a prescribed pole displacement of the rigid inclusion are deter-

mined, see Figure 4.9. Both a large and a small inclusion were

considered.

The computer program used to obtain the data for the inflation of

a unit disk was modified to allow the domain of R to be $(R_i, 1)$

as shown in Figure 4.9. The initial guess of the solution specified

the (X, Y) location of the outer edge of the inclusion. The first

element had its gradient and Hessian contributions reduced with the

following relations to enforce the boundary condition at the outer
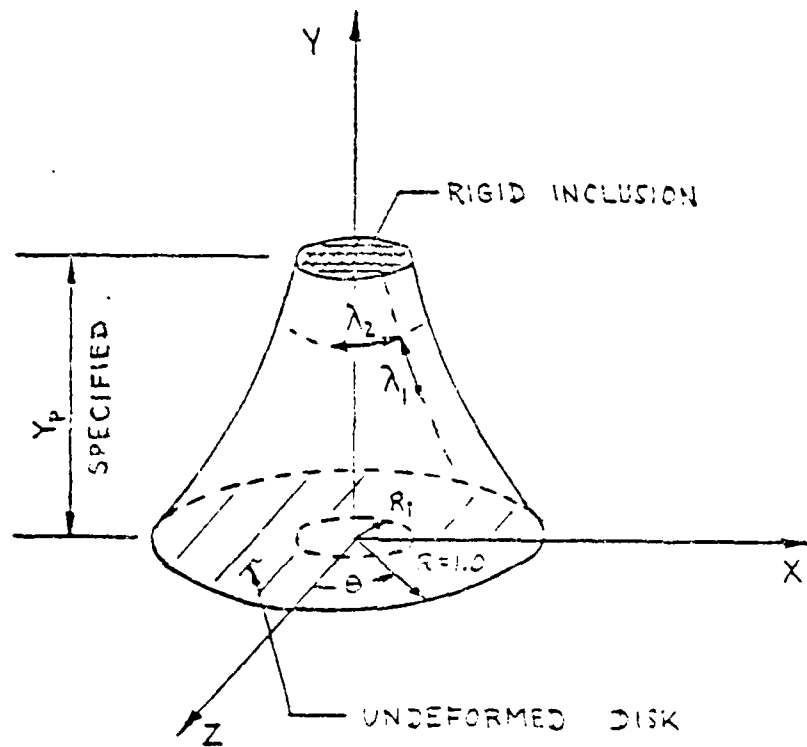
edge of the rigid inclusion.

FIGURE 4.9 DISK WITH RIGID INCLUSION.

$$
\begin{bmatrix} X_1 \\ Y_1 \\ X_2 \\ Y_2 \\ X_3 \\ Y_3 \end{bmatrix} = \begin{bmatrix} 0 & 0 & 0 & 0 \\ 0 & 0 & 0 & 0 \\ 1 & 0 & 0 & 0 \\ 0 & 1 & 0 & 0 \\ 0 & 0 & 1 & 0 \\ 0 & 0 & 0 & 1 \end{bmatrix} \begin{bmatrix} X_2 \\ Y_2 \\ X_3 \\ Y_3 \end{bmatrix} \qquad (4.4.1)
$$

The cross section profiles for the cases when the inclusion radius is 0.3 and 0.01 are shown in Figures 4.10 and 4.11. The solutions were obtained with a uniform mesh of 9 quadratic 3-node elements on the domain of R. Stretch ratios for each inclusion and two pole displacements are shown in Figures 4.12 and 4.13.
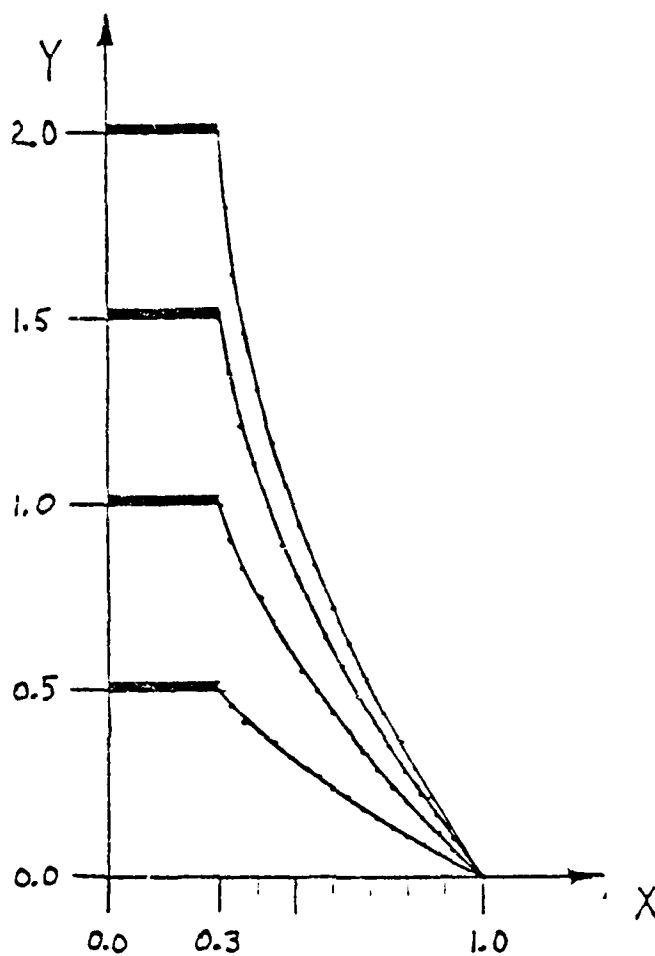
FIGURE 4.10 CROSS SECTION PROFILES
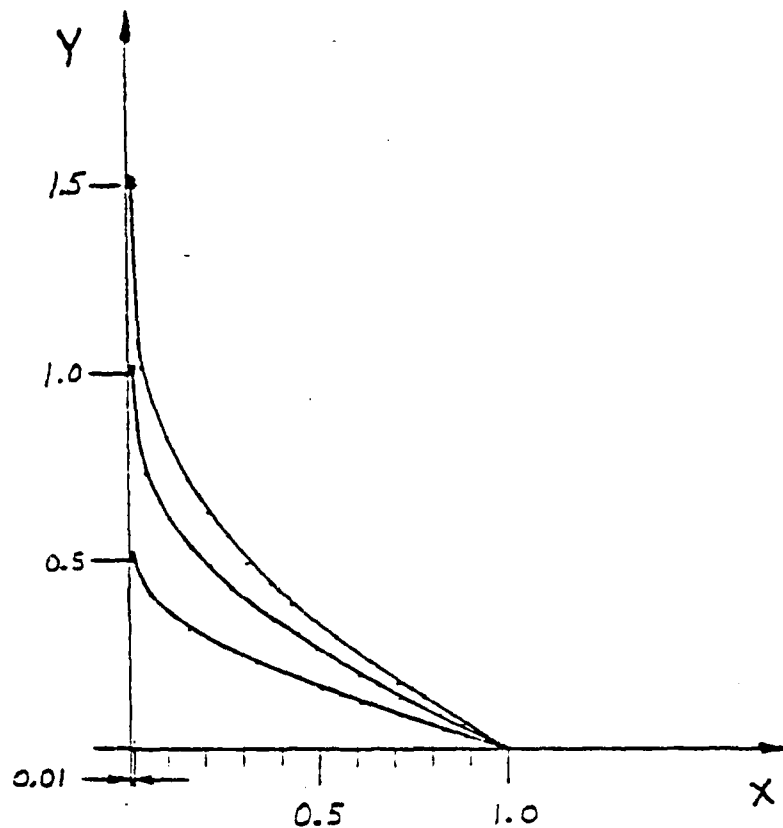FOR DISK WITH INCLUSION,
INCLUSION RADIUS = 0.3.

FIGURE 4.11 CROSS SECTION PROFILES
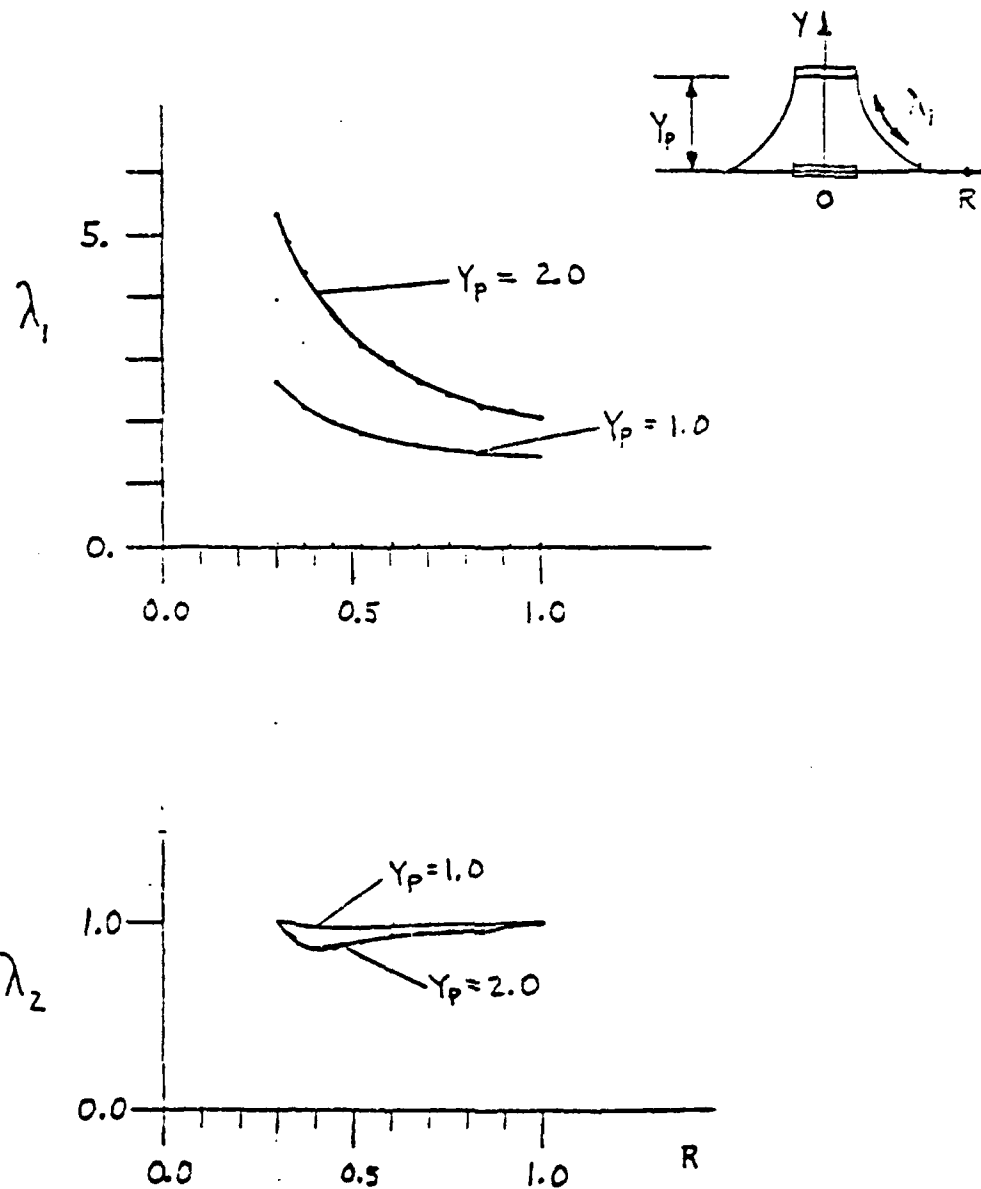FOR DISK WITH INCLUSION,
INCLUSION RADIUS = 0.01.

FIGURE 4.12 STRETCH RATIOS FOR DISK
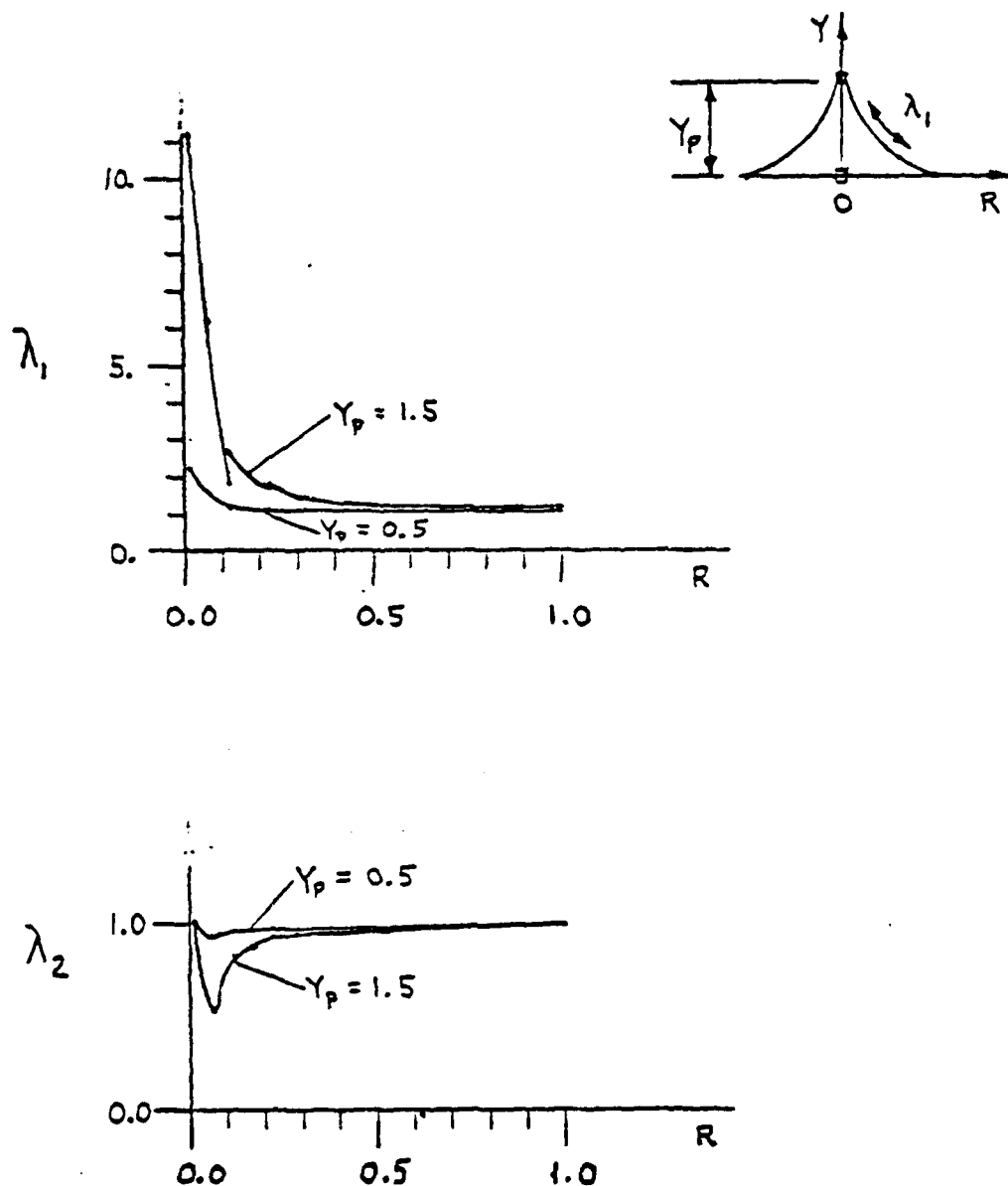WITH INCLUSION, INCLUSION
RADIUS = 0.3 .

FIGURE 4.13 STRETCH RATIOS FOR DISK
WITH INCLUSION, INCLUSION
RADIUS = 0.01 .

CHAPTER 5

INFLATION OF A TORUS

5.1 Introduction.

It is difficult to obtain analytical solutions valid for the finite inflation of a torus (see Figure 5.1) because a torus has two principal curvatures. The earliest analyses of the inflated torus involved solving stress equilibrium equations derived in the linear theory of elasticity. These solutions result in a discontinuous displacement field when the stress field is integrated. In 1963 Jordan[20] reformulated the torus problem by allowing small deformations but large derivatives of the deformations. Instead of approaching only the stress equations Jordan added the requirement that the displacement field be continuous. The material constitutive law was Hooke's law for an isotropic material in two dimensions. The formulation included defining a special "primary shape function" which allowed him to write the equilibrium equation and continuity equation in a form which could be solved by an iterative procedure. This shape function was used in later years by other investigators to aid them in their computations of approximate solutions for the nonlinear inflation (large strains) of a torus. Jordan's solution was the first solution to have a continuous displacement field. He found that his solutions for the hoop stress
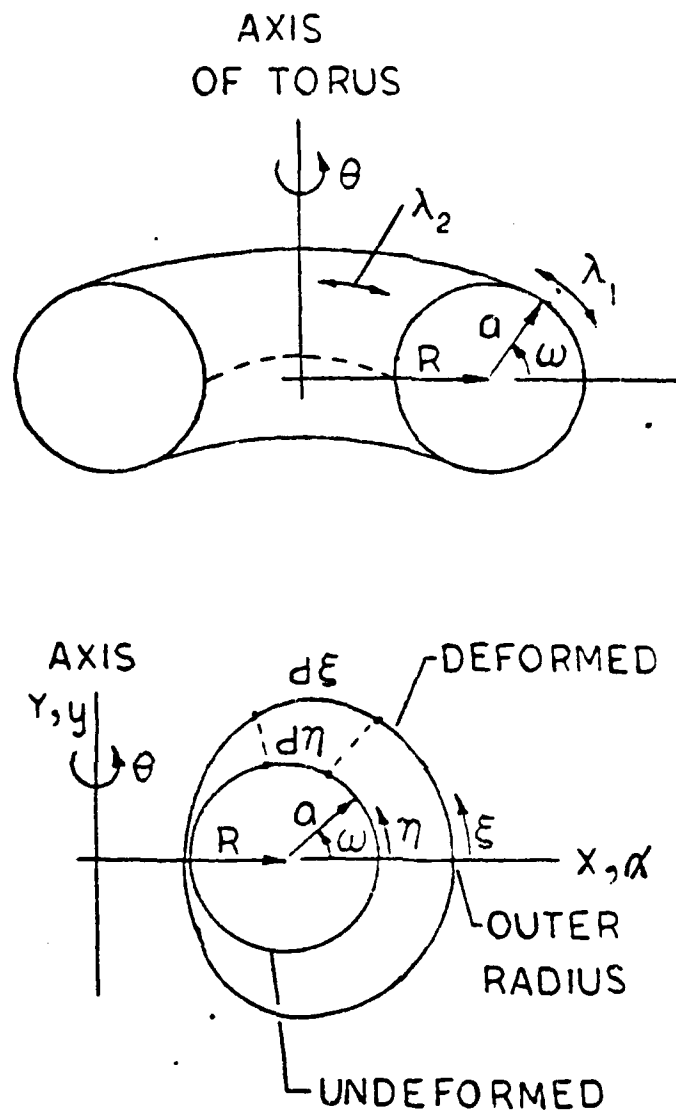
FIGURE 5.1 TORUS WITH CIRCULAR CROSS SECTION.

agree well with the earlier solutions but that the overall torus circumferential stress predicted by earlier solutions was in error by up to 18%.

In 1963 Sanders and Liepins[21] used a nonlinear membrane theory (small strains but large rotations) to formulate the nonlinear equilibrium equations for a toroidal membrane under internal pressure. The material constitutive law used is Hooke's law for an isotropic material in two dimensions. Sanders and Liepins were able to convert the nonlinear equilibrium equations into a form which could be solved by asymptotic methods. Their solutions agree well with Jordan's[20] solutions and their technique was easier to apply than Jordan's.

In 1965 Liepins[22] determined the natural vibration modes of prestressed toroidal membranes. The stresses resulting from the linear analysis of toroidal membranes were used to define the prestress state. The equations for the analysis of vibrations of prestressed membranes were reduced to a set of second order differential equations by separation of variables. The separated equations represent different forms of vibration of the torus; that is, flexural modes due to the torus bending, extensional modes of the meridional curve, etc.

Also in 1965 Kydoniefs and Spencer[23] analyzed the finite inflation of an incompressible elastic torus. They stated the theory for the

uniform inflation of a thick wall torus. Solutions were obtained for the case when the cross sectional radius of the torus is very small when compared with the overall torus radius. They presented some numerical results for the case of neo-Hookean material. Kydoniefs and Spencer suggest that since the number of exact solutions to problems in finite elasticity is small "and seems likely to remain so" that approximate solution techniques for these problems are of interest. Their interest was with the use of perturbation procedures. In particular they studied series expansions of the solution in terms of a numerically small geometric parameter (the ratio of the torus cross section radius to the overall radius of the torus). Their solutions were valid only for the case when the cross section remains circular and is small compared to the overall radius of the torus.

In 1967 Kydoniefs and Spencer[24] computed asymptotic solutions for the finite inflation of a toroidal membrane of an initially circular cross section and made of a Mooney material; see equation (1.1.5). The parameter in the asymptotic expansion was the ratio of the radius of the circular cross section to the overall radius of the torus. As a result, their solutions apply only to the case when the torus has a small cross sectional radius. They used the "shape function" introduced by Jordan[20] to help simplify the algebra.

The zero, first, and second order equations resulting from the asymptotic expansions are solved in their paper. In describing the solutions for a torus made of Mooney material Kydoniefs and Spencer indicate that there exists a pressure at which the volume of the torus will increase without bound with no further increase in pressure. In this chapter the finite element solutions indicate the same type of response for a torus with a large cross sectional radius compared to its overall radius.

5.2 Analysis of the Inflation of a Torus of Circular Cross Section.

The deformations resulting from the inflation of a torus which has a circular cross section in its undeformed state (see Figure 5.1) are analyzed in this section. The Mooney form of the strain energy as given in equation (1.1.5) is used with $C_1 = 1.0$ and $\alpha = 0.1$. The cross section radius a = 0.5 and the overall radius of the torus R = 1.0. The rectangular coordinates of the undeformed torus are (x, y) and of the deformed torus are (X, Y) as shown in Figure 5.1. Using the angular coordinate ω as the independent variable and considering the symmetry we determine that the domain $0 \leq \omega \leq \pi$ must be discretized. The boundary conditions are

$$Y(\omega = 0, \pi) = 0$$

and
$$\left.\frac{dX}{d\omega}\right|_{\omega=0,\pi} = 0 \qquad\qquad (5.2.1)$$

Using the parametric coordinates η and ξ to measure the arc length of the undeformed and deformed meridional curve respectively, the meridional stretch ratio, λ_1, and the circumferential stretch ratio, λ_2, can be computed. They are given by the following expressions

$$\lambda_1 = \frac{d\xi}{d\eta} \qquad\qquad \lambda_2 = \frac{X}{\chi} \qquad\qquad (5.2.2)$$

If we let $\dfrac{d(\cdot)}{d\omega} = (\cdot)'$ the expressions for λ_1^2 and λ_2^2 in terms of X, Y and ω become

$$\lambda_1^2 = \frac{(X')^2 + (Y')^2}{a^2}$$

$$\lambda_2^2 = \frac{X^2}{(R + a \cos\omega)^2} \qquad\qquad (5.2.3)$$

and
$$\lambda_3^2 = \frac{1}{\lambda_1^2 \, \lambda_2^2}$$

When we use the quadratic elements the boundary conditions expressed
by equations (5.2.1) yield the following relations among the nodal
variables for the first and last elements on the domain $0 \le \omega \le \pi$

$$
\begin{bmatrix} X_1 \\ Y_1 \\ X_2 \\ Y_2 \\ X_3 \\ Y_3 \end{bmatrix} =
\begin{bmatrix}
\frac{4}{3} & 0 & -\frac{1}{3} & 0 \\
0 & 0 & 0 & 0 \\
1 & 0 & 0 & 0 \\
0 & 1 & 0 & 0 \\
0 & 0 & 1 & 0 \\
0 & 0 & 0 & 1
\end{bmatrix}
\begin{bmatrix} X_2 \\ Y_2 \\ X_3 \\ Y_3 \end{bmatrix}
\qquad (5.2.4)
$$

and

$$
\begin{bmatrix} X_{N-2} \\ Y_{N-2} \\ X_{N-1} \\ Y_{N-1} \\ X_N \\ Y_N \end{bmatrix} =
\begin{bmatrix}
1 & 0 & 0 & 0 \\
0 & 1 & 0 & 0 \\
0 & 0 & 1 & 0 \\
0 & 0 & 0 & 1 \\
-\frac{1}{3} & 0 & \frac{4}{3} & 0 \\
0 & 0 & 0 & 0
\end{bmatrix}
\begin{bmatrix} X_{N-2} \\ Y_{N-2} \\ X_{N-1} \\ Y_{N-1} \end{bmatrix}
\qquad (5.2.5)
$$

the last node number.

cubic elements are used the boundary conditions yield

$$
\begin{bmatrix} X_1 \\ X_1' \\ Y_1 \\ Y_1' \\ X_2 \\ X_2' \\ Y_2 \\ Y_2' \end{bmatrix} =
\begin{bmatrix}
1 & 0 & 0 & 0 & 0 & 0 \\
0 & 0 & 0 & 0 & 0 & 0 \\
0 & 0 & 0 & 0 & 0 & 0 \\
0 & 1 & 0 & 0 & 0 & 0 \\
0 & 0 & 1 & 0 & 0 & 0 \\
0 & 0 & 0 & 1 & 0 & 0 \\
0 & 0 & 0 & 0 & 1 & 0 \\
0 & 0 & 0 & 0 & 0 & 1
\end{bmatrix}
\begin{bmatrix} X_1 \\ Y_1' \\ X_2 \\ X_2' \\ Y_2 \\ Y_2' \end{bmatrix}
\qquad (5.2.6)
$$

and

$$
\begin{bmatrix} X_{N-1} \\ X_{N-1}' \\ Y_{N-1} \\ Y_{N-1}' \\ X_N \\ X_N' \\ {} \\ Y_N' \end{bmatrix} =
\begin{bmatrix}
{} & 0 & 0 & 0 & 0 & 0 \\
0 & 1 & 0 & 0 & 0 & 0 \\
0 & 0 & 1 & 0 & 0 & 0 \\
0 & 0 & 0 & 1 & 0 & 0 \\
0 & 0 & 0 & 0 & 1 & 0 \\
0 & 0 & 0 & 0 & 0 & 0 \\
0 & 0 & 0 & 0 & 0 & 0 \\
0 & 0 & 0 & 0 & 0 & 1
\end{bmatrix}
\begin{bmatrix} X_{N-1} \\ X_{N-1}' \\ Y_{N-1} \\ Y_{N-1}' \\ X_N \\ Y_N' \end{bmatrix}
\qquad (5.2.7)
$$

The first and last element contributions to the gradient and Hessian are appropriately modified with relations (5.2.4) to (5.2.7) as shown in Chapter 2.

The work, W , done by the pressure, P , during the deformation is

$$W = \int P\,dV = 4\pi P \int_{\omega=\pi}^{0} X\,Y\,\frac{dX}{d\omega}\,d\omega - PV_o \qquad (5.2.8)$$

where V_o = the initial volume of the torus. Dropping the constant term since it does not contribute to the gradient or Hessian and changing the integration limits we have

$$W = -4\pi P \int_{\omega=0}^{\pi} X\,Y\,X'\,d\omega \qquad (5.2.9)$$

Using $d\left(\tfrac{1}{2}X^2\right) = XX'\,d\omega$, integrating by parts, and remembering that $Y(\omega=0,\pi) = 0$ we obtain

$$W = 2\pi P \int_{\omega=0}^{\pi} X^2\,Y'\,d\omega \qquad (5.2.10)$$
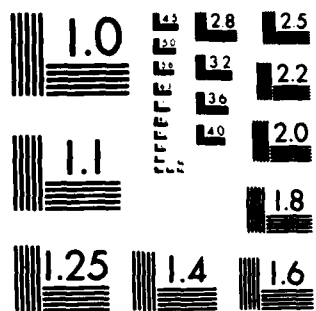
MICROCOPY RESOLUTION TEST CHART

NATIONAL BUREAU OF STANDARDS-1963-A

and
$$W_e = 2\pi P \int_{(e)} X^2 Y' \, d\omega \tag{5.2.11}$$

where W_e = the contribution to the work from element (e).

Expression (5.2.11) is identical in form to (4.2.10) and after some algebra we obtain the following element contributions to the gradient and the Hessian

$$\frac{\partial W_e}{\partial \{u\}_e^T} = 2\pi P \sum_{i=1}^{P} \omega_i \left(2X_i \dot{Y}_i \{\varphi_i\} + X_i^2 \{\psi_i\} \right) \tag{5.2.12}$$

and

$$\frac{\partial^2 W_e}{\partial \{u\}_e \partial \{u\}_e^T} = 4\pi P \sum_{i=1}^{P} \omega_i \left[X_i \left(\{\varphi_i\}\{\psi_i\}^T + \{\psi_i\}\{\varphi_i\}^T \right) \right. \tag{5.2.13}$$
$$\left. + \dot{Y}_i \{\varphi_i\}\{\varphi_i\}^T \right]$$

The expressions for the stretch ratios λ_1, λ_2, and λ_3 in equations (5.2.3) were used with the boundary conditions shown in (5.2.4) to (5.2.7), and the contributions from the work shown in (5.2.12) and (5.2.13) in the finite element algorithm outlined in

Chapter 2 to compute the deformation of the torus as a function of pressure. The computer program was written in double precision. The cross sectional profiles of the inflated torus are shown in Figure 5.2. It was found that the inner circumferential radius of the torus decreases slowly with increasing pressure while the outer circumferential radius increases rapidly with increasing pressure, see Figure 5.3. The distribution of the stretch ratios and strain invariants for three values of the pressure are shown in Figures 5.4 and 5.5. In the paper by Kydoniefs and Spencer[24] the following expressions for the membrane stresses are presented (here the initial membrane thickness, h_o, is assumed to be 1.0).

$$T_1 = 4\lambda_3 \left(\lambda_1^2 - \lambda_3^2 \right) \left(\frac{\partial W}{\partial I_1} + \lambda_2^2 \frac{\partial W}{\partial I_2} \right)$$

$$T_2 = 4\lambda_3 \left(\lambda_2^2 - \lambda_3^2 \right) \left(\frac{\partial W}{\partial I_1} + \lambda_1^2 \frac{\partial W}{\partial I_2} \right)$$

$$(5.2.14)$$

The stress distributions for three values of the pressure were computed using (5.2.14) and are shown in Figure 5.6.

The maximum values of T_1 and T_2 were computed for a series of values of pressure and the results are shown in Figure 5.7.
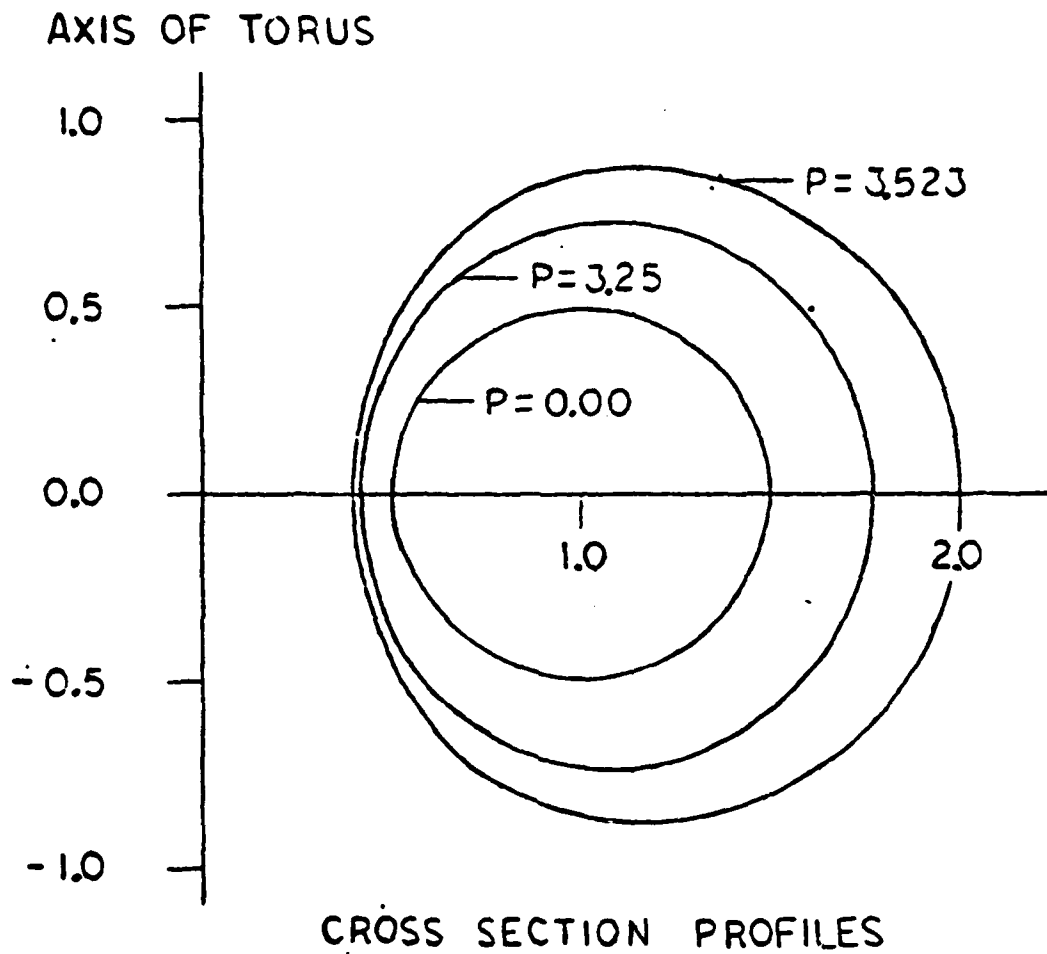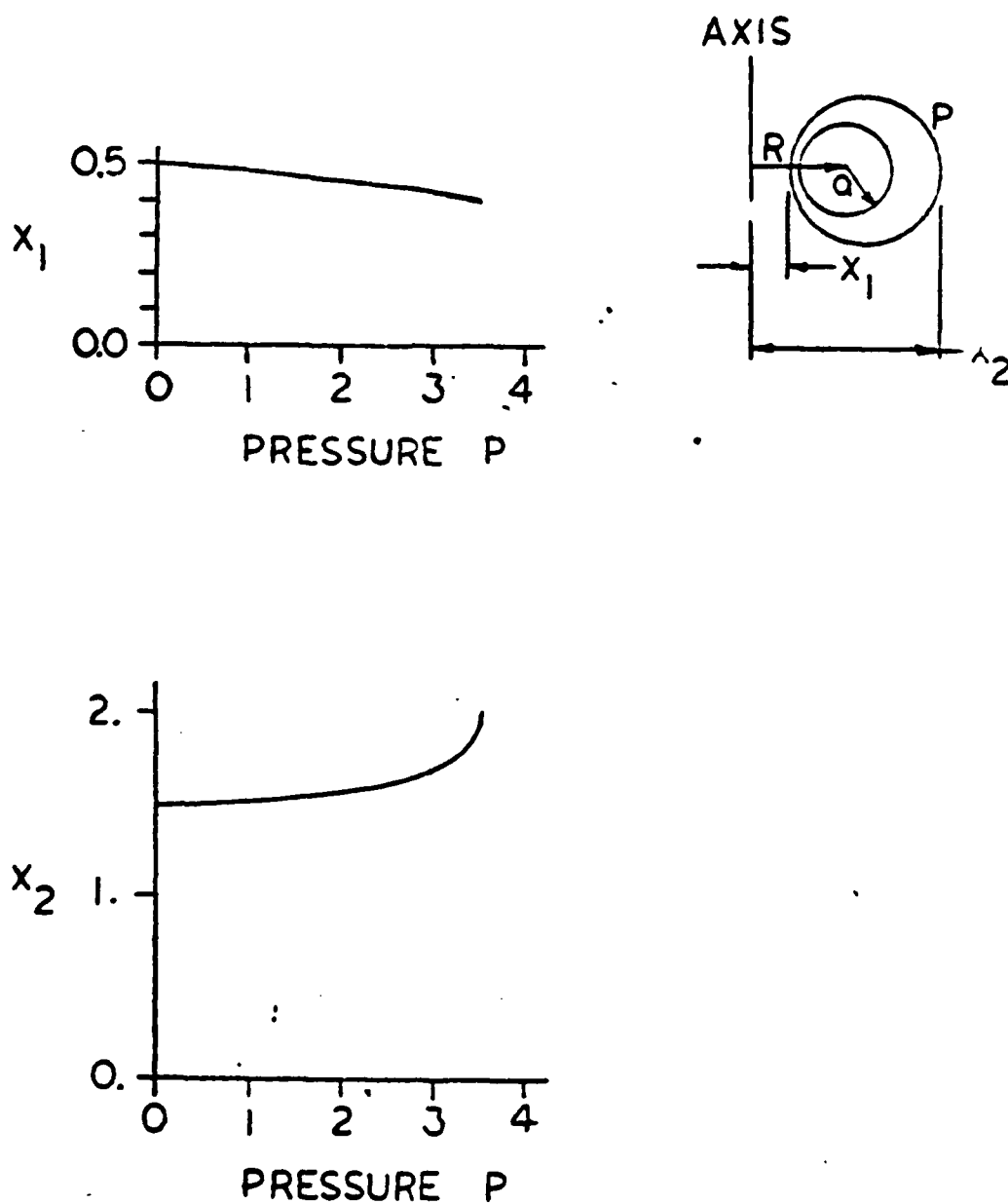
FIGURE 5.2   INFLATION OF TORUS.

FIGURE 5.3 INNER AND OUTER TORUS
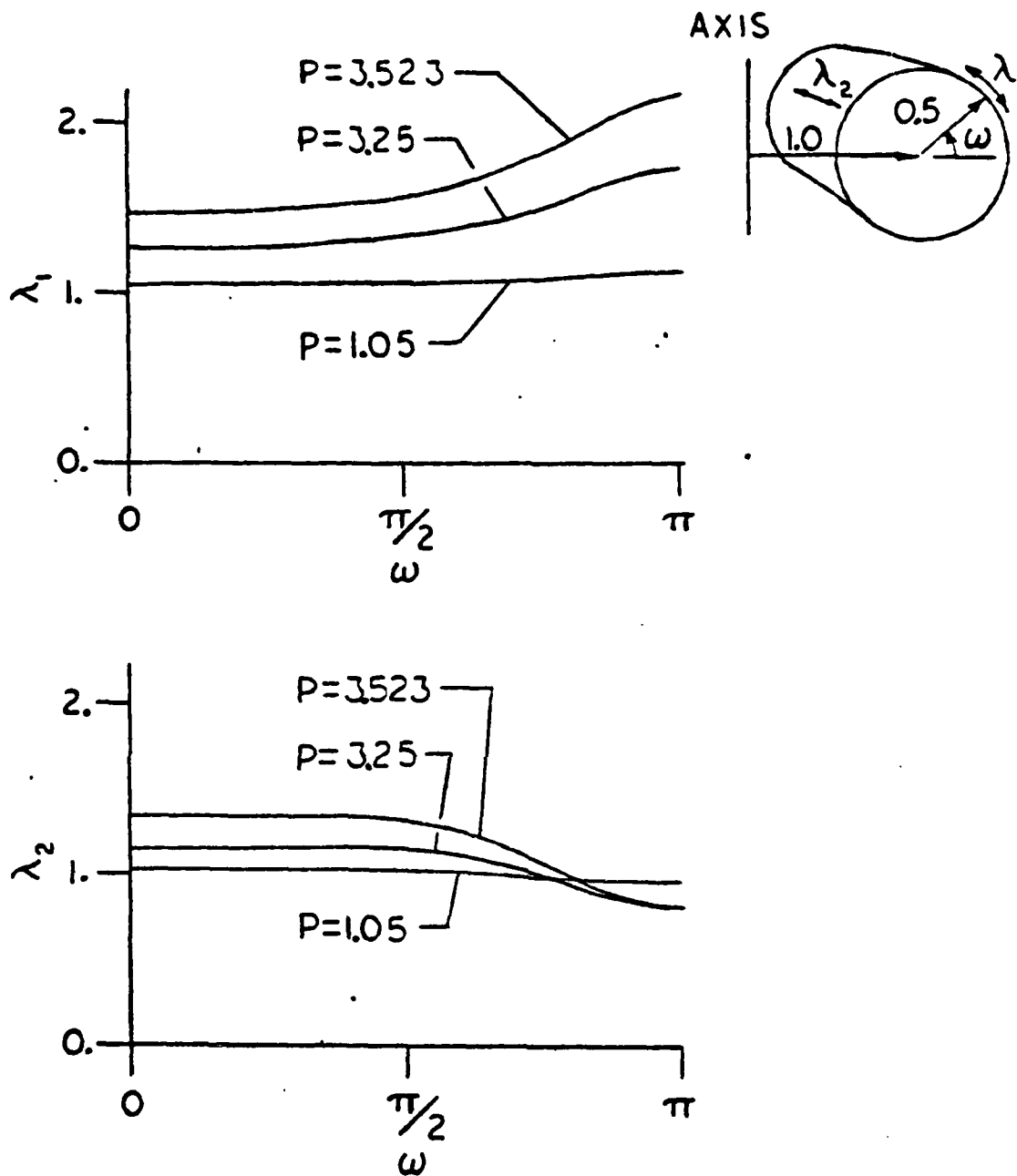RADII VS PRESSURE.

FIGURE 5.4 STRETCH RATIOS FOR
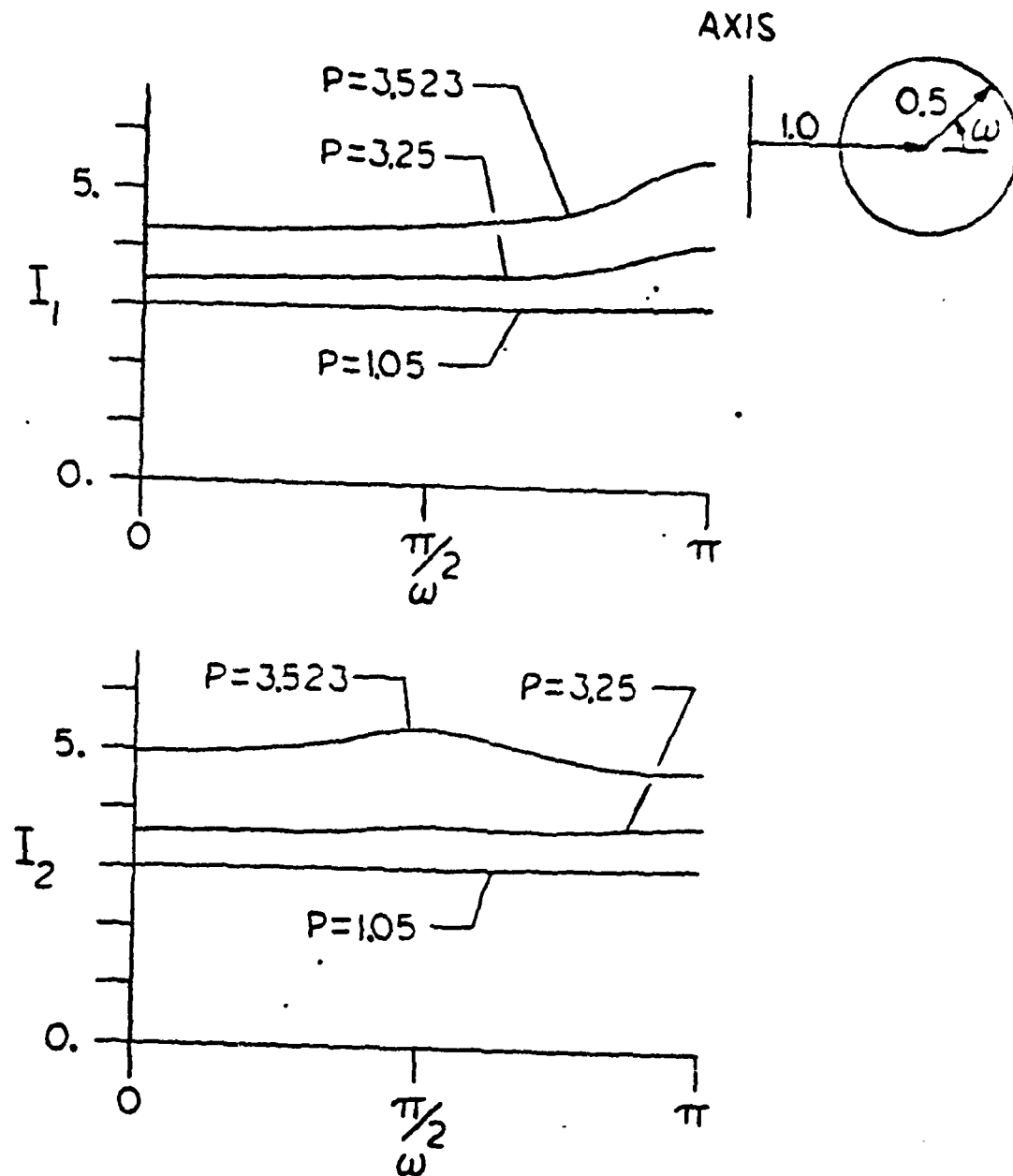INFLATION OF TORUS.

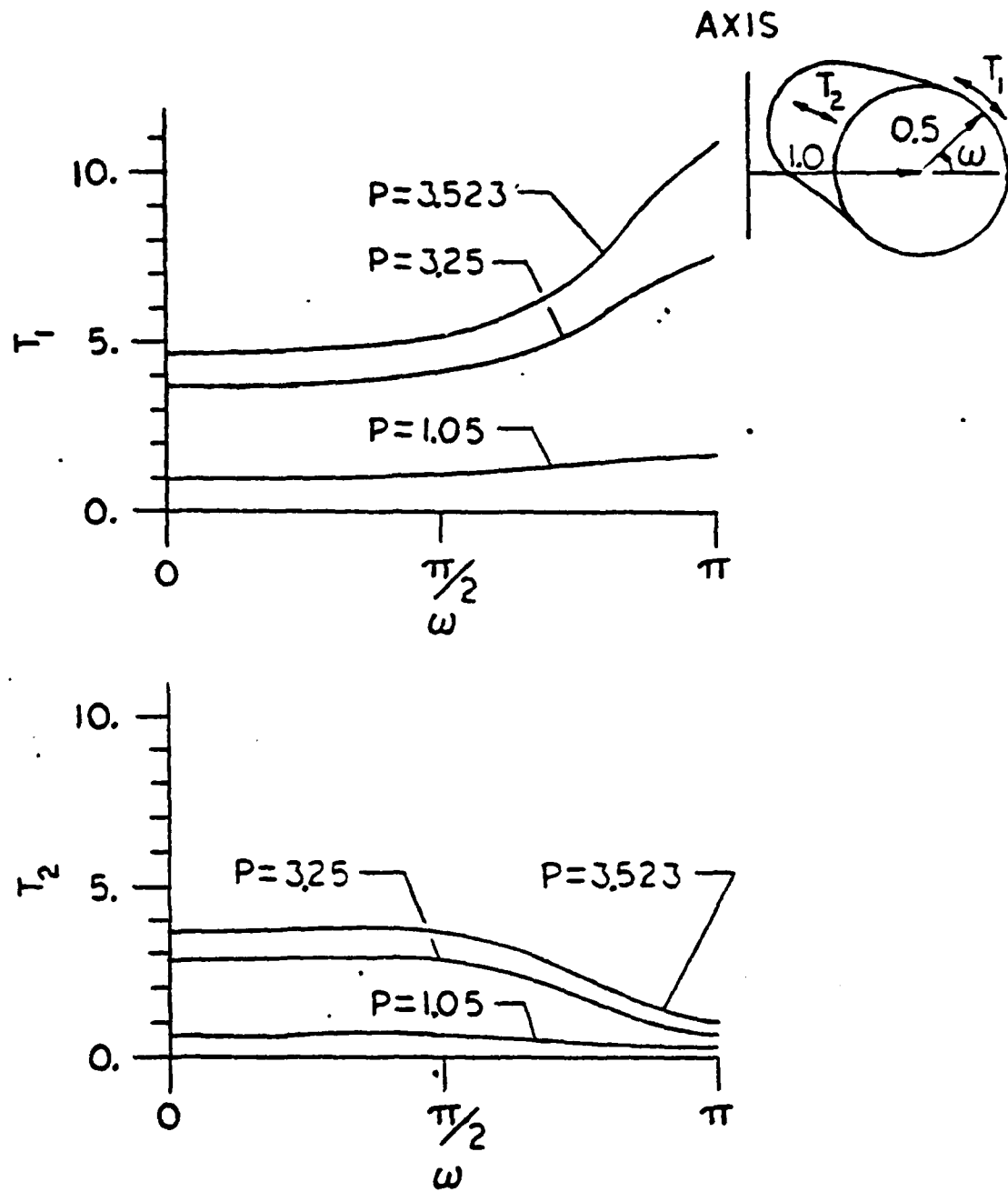FIGURE 5.5 STRAIN INVARIANTS FOR INFLATION OF TORUS.

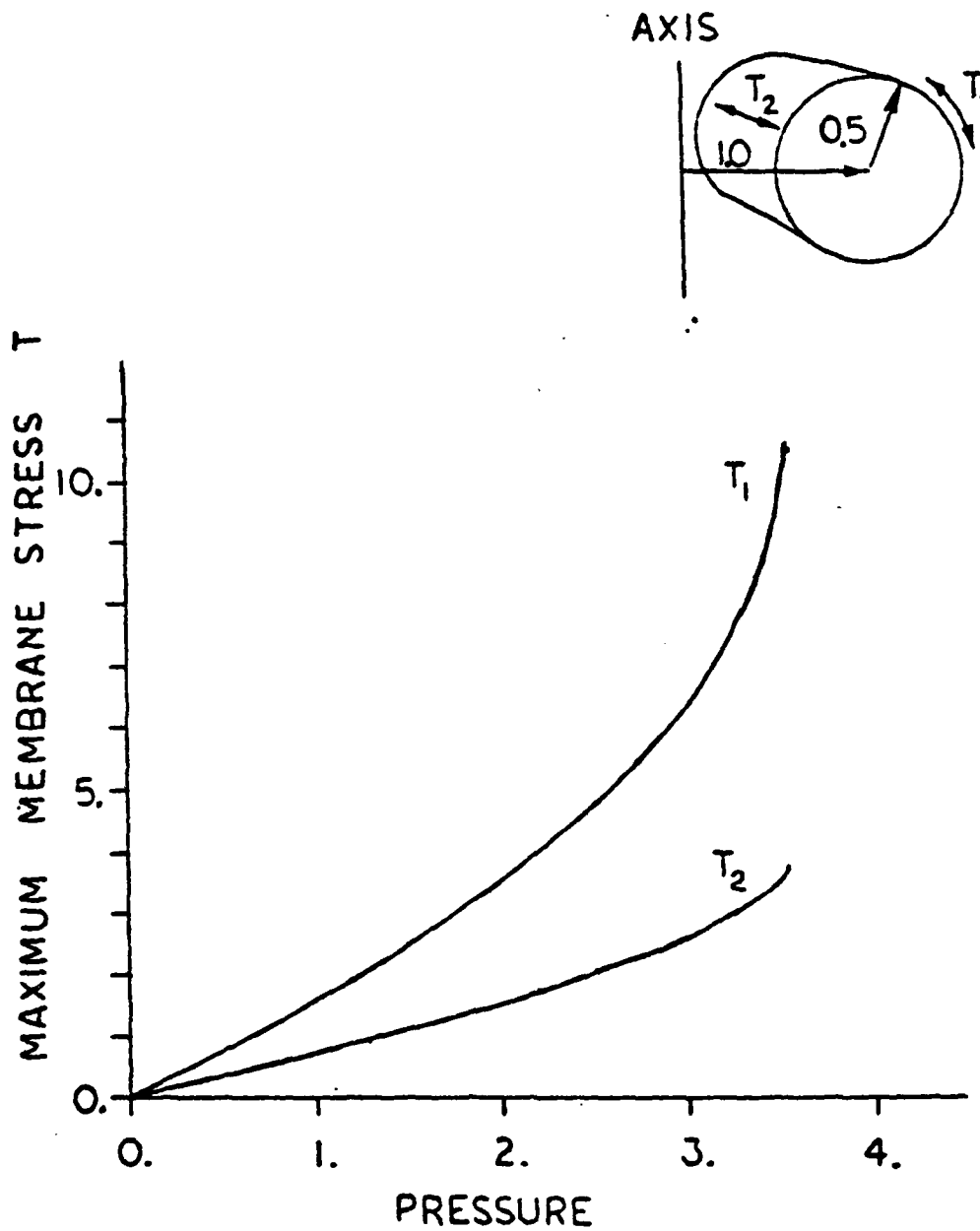FIGURE 5.6 STRESS RESULTANTS FOR INFLATION OF TORUS.

FIGURE 5.7 INFLATION OF TORUS,
MAX MEMBRANE STRESS
VS PRESSURE.

When the pressure increased beyond $P = 3.50$ it became difficult

to use the incremental pressure formulation to find configurations at

successively higher pressures. As a result, the computations were

stopped at $P = 3.523$. This behavior was suggested by

Kydoniefs and Spencer[24] when they determined asymptotic solutions

for the inflation of a torus with a small cross section and made of

Mooney material.

5.3 Convergence of the Finite Element Solutions.

The convergence of the displacements, strain energy, and the

lowest eigenvalue of the Hessian of the potential energy are examined

in this section. As in section 3.3 convergence was assumed to follow a

power law with respect to mesh size as shown in equation (3.3.1). The

outer overall circumferential radius of the torus and the total strain

energy were determined for a series of mesh sizes. The quadratic

element was used with 2- and 4-point integration and the cubic element

was used with 3-, 4-, and 6-point integration (2-point integration

with the cubic elements resulted in a reduced rank Hessian). The

finite element programs written to obtain the data used in this section

were written in double precision. Table 5.1 shows the convergence of

the outer radius and the strain energy when quadratic elements are used.

The results indicated that both 2- and 4-point Gauss-Legendre

TABLE 5.1 Convergence Data for Inflation of Torus, Quadratic

Elements

Outer Radius (P = 3.25)

No. of Integration Points	3 Elements	6 Elements	9 Elements	Converged
2	1.7538039	1.7591435	1.7593895	1.7594454
4	1.7541697	1.7591665	1.7593966	1.7594489

Strain Energy (P = 3.25)

No. of Integration Points	3 Elements	6 Elements	9 Elements	Converged
2	12.589861	12.689202	12.692323	12.692851
4	12.687924	12.695023	12.693598	---

integration gave comparable accuracy when the quadratic element was used. Table 5.2 indicates similar results when cubic elements were used. In fact, to eight significant digits there were no differences in the computed displacements for the cases of 4- and 6-point integration when the cubic elements were used. The converged values of the outer radius and strain energy were identical to eight significant digits for 3-, 4-, and 6-point integration with cubic elements. Thus, the data in Tables 5.1 and 5.2 indicates that using an integration scheme of higher order than required for a full rank Hessian is wasteful on these problems.

Figures 5.8 and 5.9 summarize the accuracy of the integration schemes used. These figures are not intended for comparing the efficiency of the cubic element vs the quadratic elements since the total degrees of freedom are not accounted for in these figures. However, comparable convergence rates were obtained for both the quadratic and cubic elements. This is surprising since in linear elliptic problems this convergence rate is dependent on the order of the interpolation polynomials (see reference 8).

The eigenvalues of the Hessian were investigated and the data is presented in Table 5.3. The Hessian was positive definite at the solution $\left(\|g\| \leq 10^{-8} \right)$ for all mesh sizes and for all

TABLE 5.2   Convergence Data for Inflation of Torus, Cubic Elements

Outer Radius (P = 3.25)

No. of Integration Points	4 Elements	8 Elements	12 Elements	Converged
3	1.7596120	1.7594601	1.7594520	1.7594500
4	1.7596131	1.7594602	1.7594520	1.7594500
6	1.7596131	1.7594602	1.7594520	1.7594500

Strain Energy (P = 3.25)

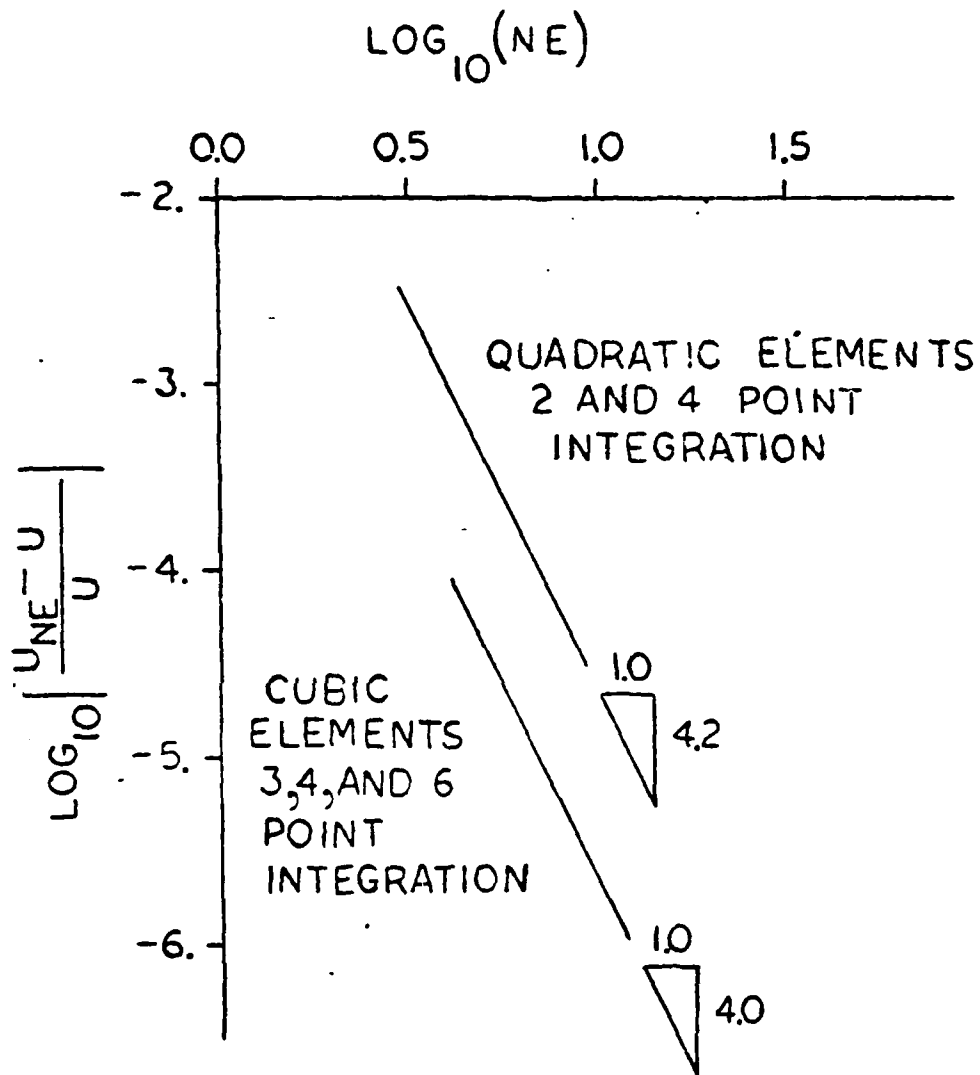| No. of Integration Points	4 Elements	8 Elements	12 Elements	Converged
3	12.692719	12.693058	12.693070	12.693072
4	12.691811	12.693046	12.693069	12.693072
6	12.691827	12.693046	12.693069	12.693072

FIGURE 5.8 CONVERGENCE OF OUTER
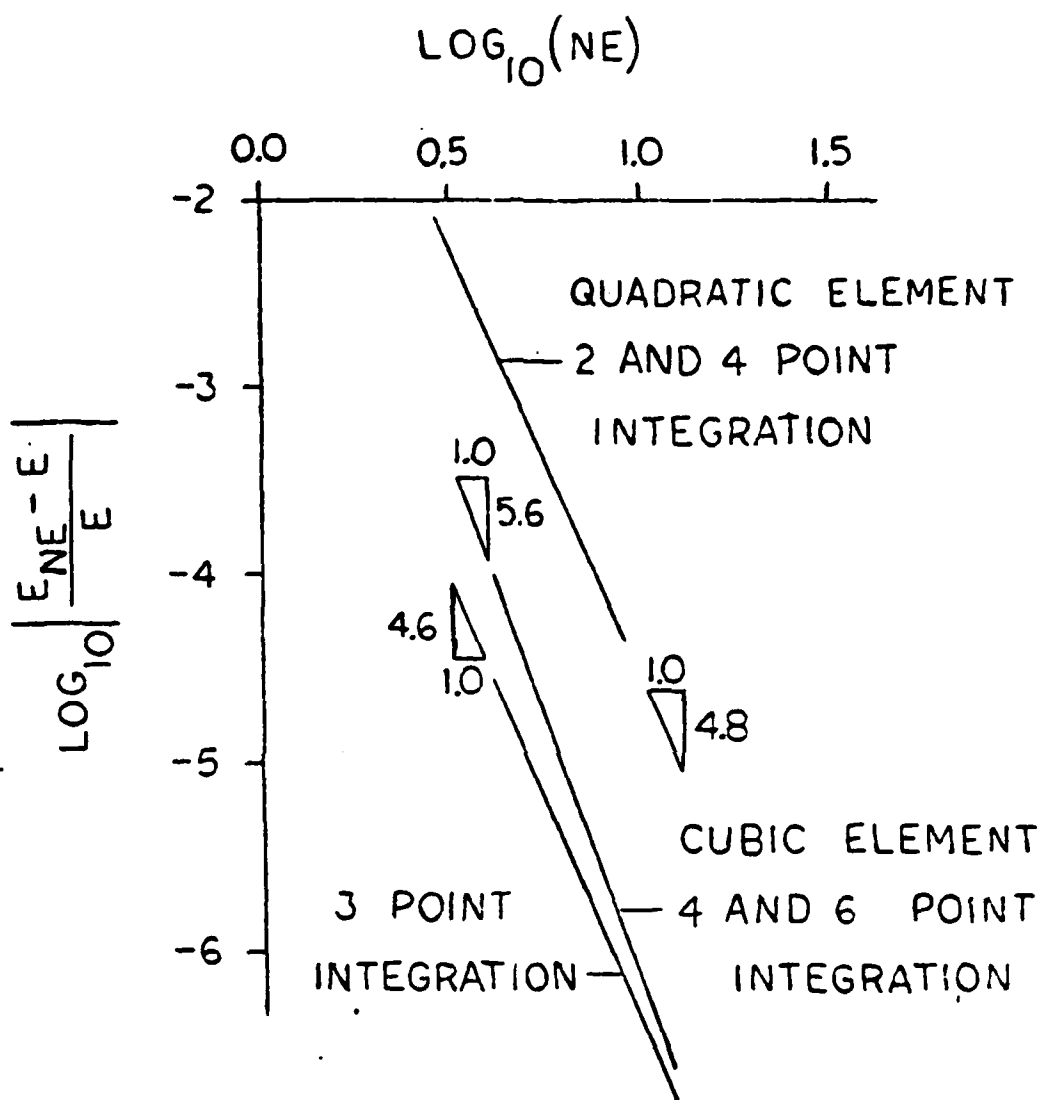RADIUS-INFLATION OF
TORUS.

FIGURE 5.9 CONVERGENCE OF STRAIN ENERGY - INFLATION OF TORUS.

TABLE 5.3   Convergence Data for Inflation of Torus, Lowest Eigen-
            value of Hessian

Quadratic Elements   (P = 3.25)

No. of Integration Points	3 Elements	6 Elements	9 Elements	Converged
2	15.969049	7.3660452	4.8047576	0.0507
4	16.060752	7.3717412	4.8055225	0.6935

Cubic Elements   (P = 3.25)

No. of Integration Points	4 Elements	8 Elements	12 Elements	Converged
3	3.3165205	1.6808296	1.1262479	-0.0249
4	3.3219768	1.6825444	1.1269123	-0.0267
6	3.3209281	1.6824904	1.1269044	-0.0262

integration orders. However, if the eigenvalues are assumed to be converging according to a power law with respect to mesh size, only the quadratic element is associated with a positive definite converged solution.

5.4 Analysis of the Inflation of a Torus of Elliptical Cross Section.

This section describes a finite element analysis of the inflation of a torus with an elliptical cross section in its undeformed state. The torus is assumed to have its center at $X = R$, semimajor axis in the x direction of value "a", and a semiminor axis in the y direction of value "b" (see Figures 5.1 and 5.10). Following the analysis of section 5.2 and taking the geometry of the ellipse into account in the calculations the following form of the stretch ratios are obtained.

$$\lambda_1^2 = \frac{(X')^2 + (Y')^2}{\left[\rho^2 + \frac{\rho^6 (a^2 - b^2)^2 \sin^2 \omega \cos^2 \omega}{a^4 b^4} \right]} \tag{5.4.1}$$
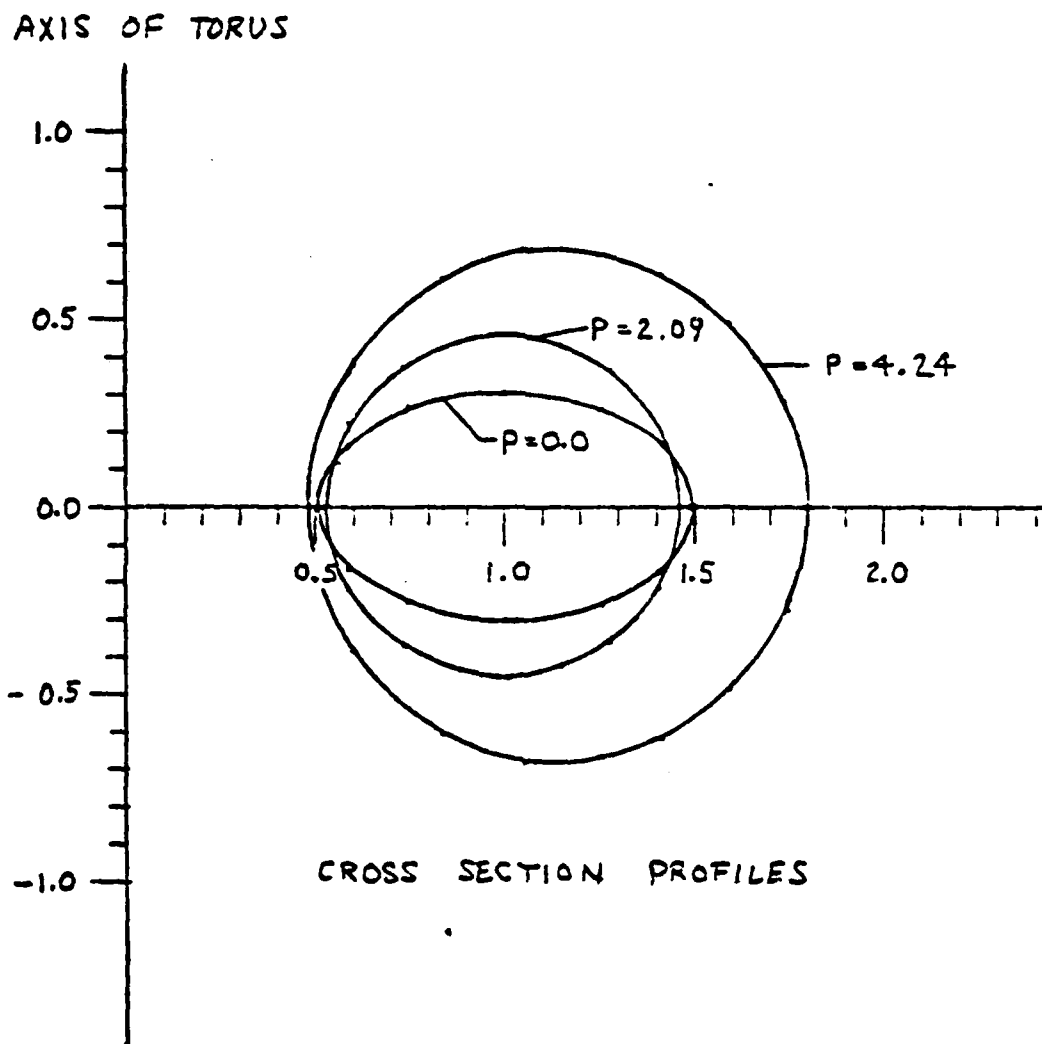
$$\lambda_2^2 = \frac{X^2}{\left[R + \rho \cos \omega \right]^2} \tag{5.4.2}$$

AXIS OF TORUS

1.0

0.5

P=2.09

P=4.24

P=0.0

0.0

0.5   1.0   1.5   2.0

-0.5

CROSS   SECTION   PROFILES

-1.0

FIGURE 5.10   INFLATION   OF A TORUS
WITH AN ELLIPTICAL
CROSS SECTION.

where
$$\rho = \cfrac{1}{\cfrac{\cos^2\omega}{a^2} + \cfrac{\sin^2\omega}{b^2}}$$

The third stretch ratio is given by the condition that $\lambda_1 \lambda_2 \lambda_3 = 1$.
The expression used for computing the work done by the pressure when
a torus with a circular cross section is inflated applies here also.
This is true because the only difference in the work expressions is a
constant term which does not contribute to the gradient or the Hessian.

The finite element program written to analyze the torus with a
circular cross section using cubic elements was modified using expres-
sions (5.4.1) and (5.4.2). Another minor modification of the program
was required to represent integration on a torus with an elliptical
cross section instead of a circular cross section. The case of a
semimajor axis equal to 0.5 and a semiminor axis equal to 0.3 was
analyzed. The cross section profiles are shown in Figure 5.10. The
elliptical cross section very quickly converted to a near circular
cross section when the pressure was increased from 0.0 to about 1.35.
In fact, at low pressures $\left(P < 1.35 \right)$ the solutions obtained
could not be considered to apply to a thin rubber membrane since a
compressive membrane stress was computed in the circumferential direc-
tion on the outermost portions of the torus.

After a pressure of 1.35 was reached many of the characteristics
of the deformation were similar to the case of a torus with a circular
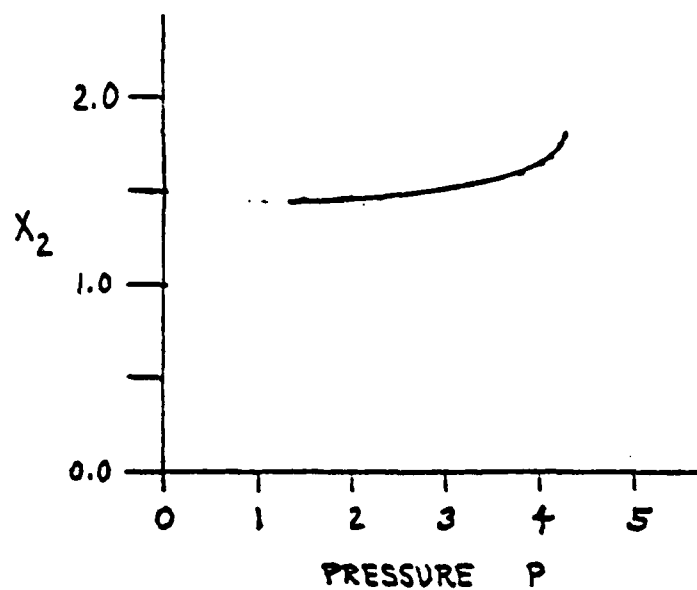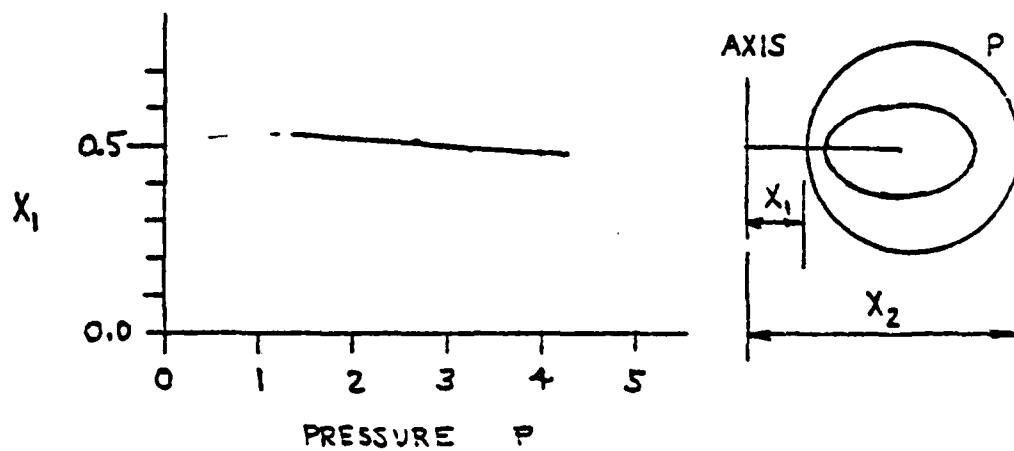cross section. Figure 5.11 indicates that the innermost and outermost

FIGURE 5.11   INNER AND OUTER TORUS
RADII   VS PRESSURE FOR
ELLIPTICAL CROSS SECTION.

circumferential radii tend to initially change magnitude in the opposite sense from the case for a circular cross section. Eventually, however, these radii follow the same type of pattern as shown in Figure 5.3. When the pressure was large enough $\left(\underline{P} > 2.09 \right)$ to cause $\lambda_1 > 1.10$ everywhere the cross section profile was nearly circular and Figures 5.12 to 5.15 indicate that the stretch ratios, strain invariants and stresses have profiles that are similar to the corresponding profiles for the torus with a circular cross section shown in Figures 5.4 to 5.7.
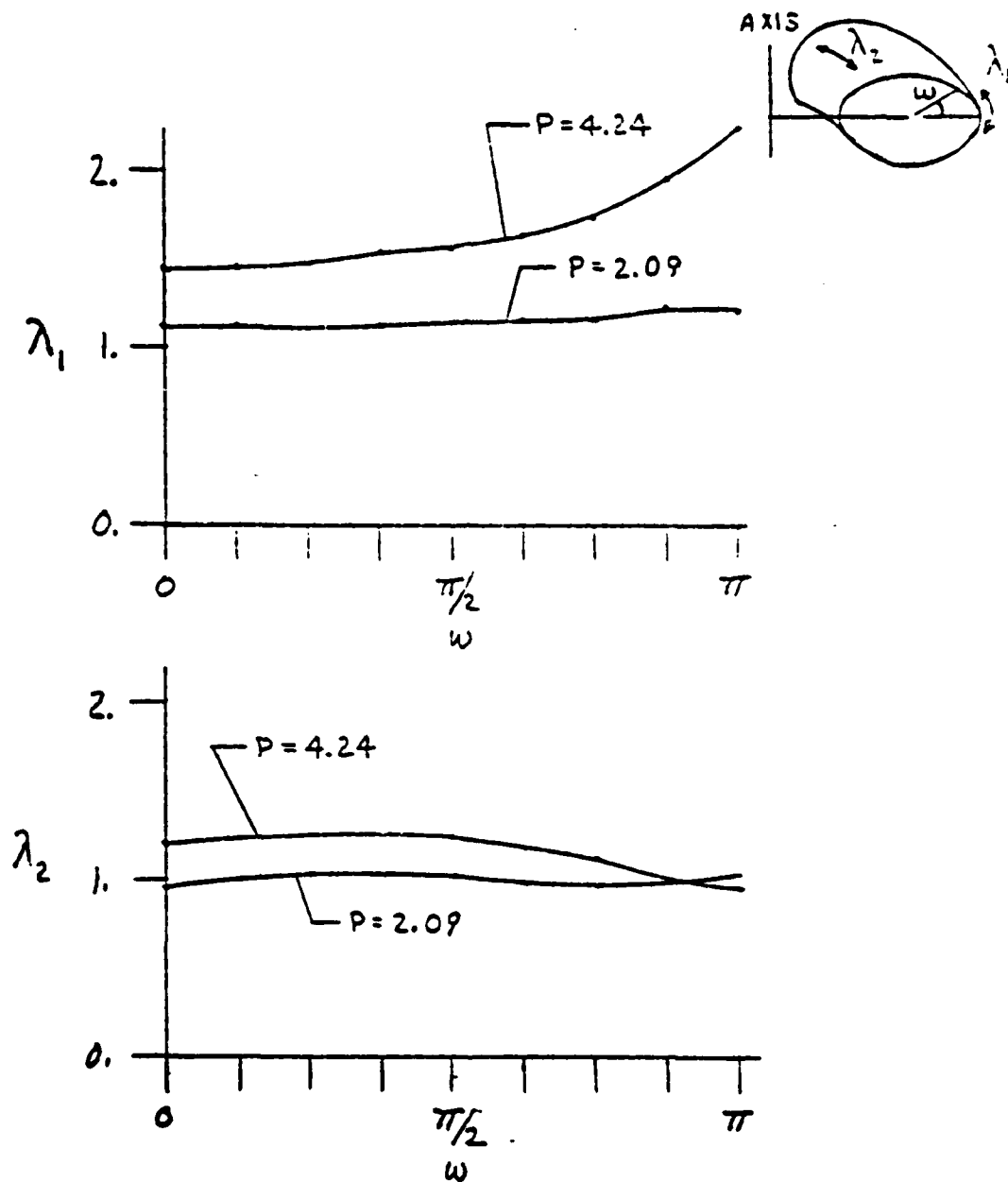
FIGURE 5.12 STRETCH RATIOS FOR TORUS WITH ELLIPTICAL CROSS SECTION.
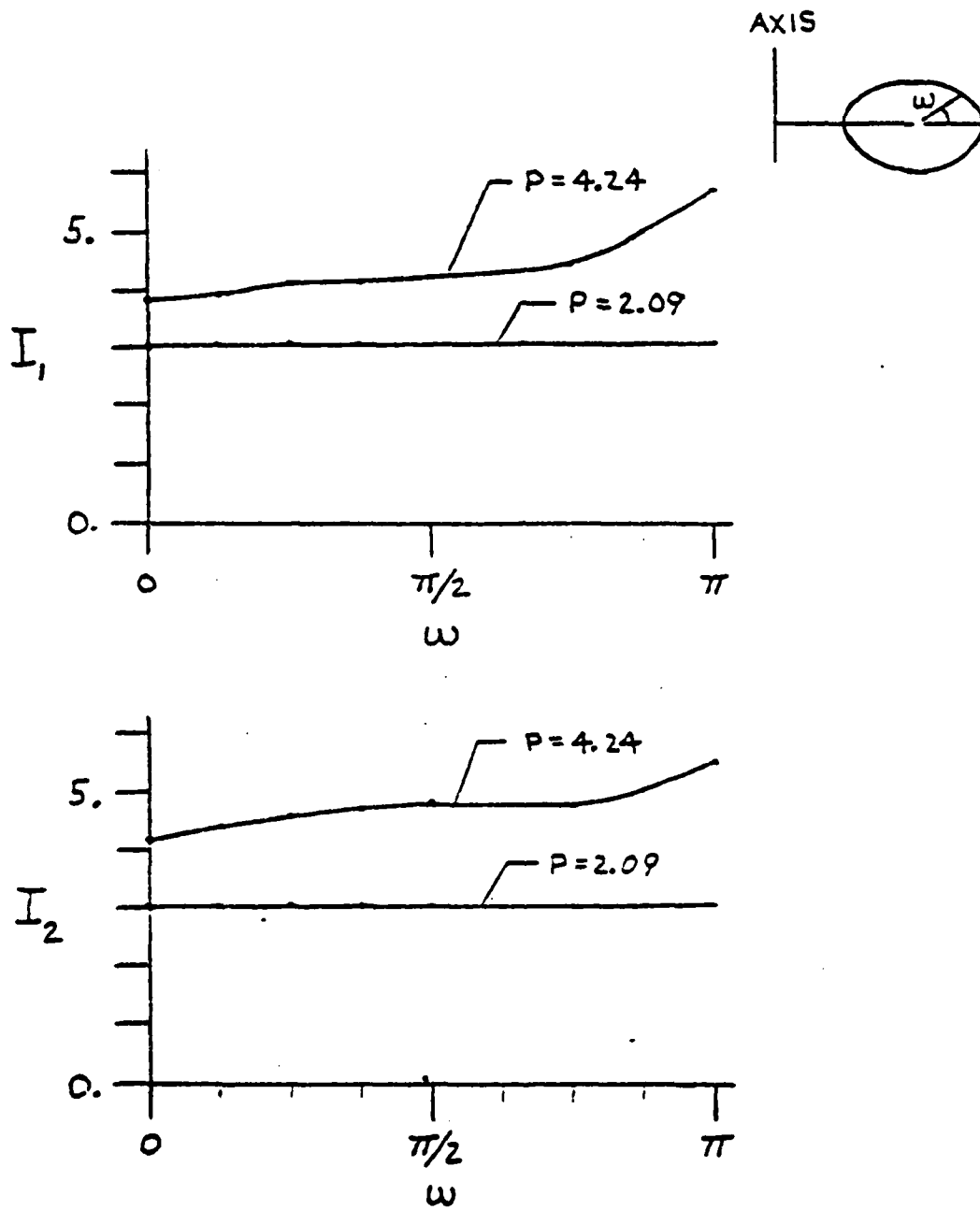
FIGURE 5.13 STRAIN INVARIANTS FOR
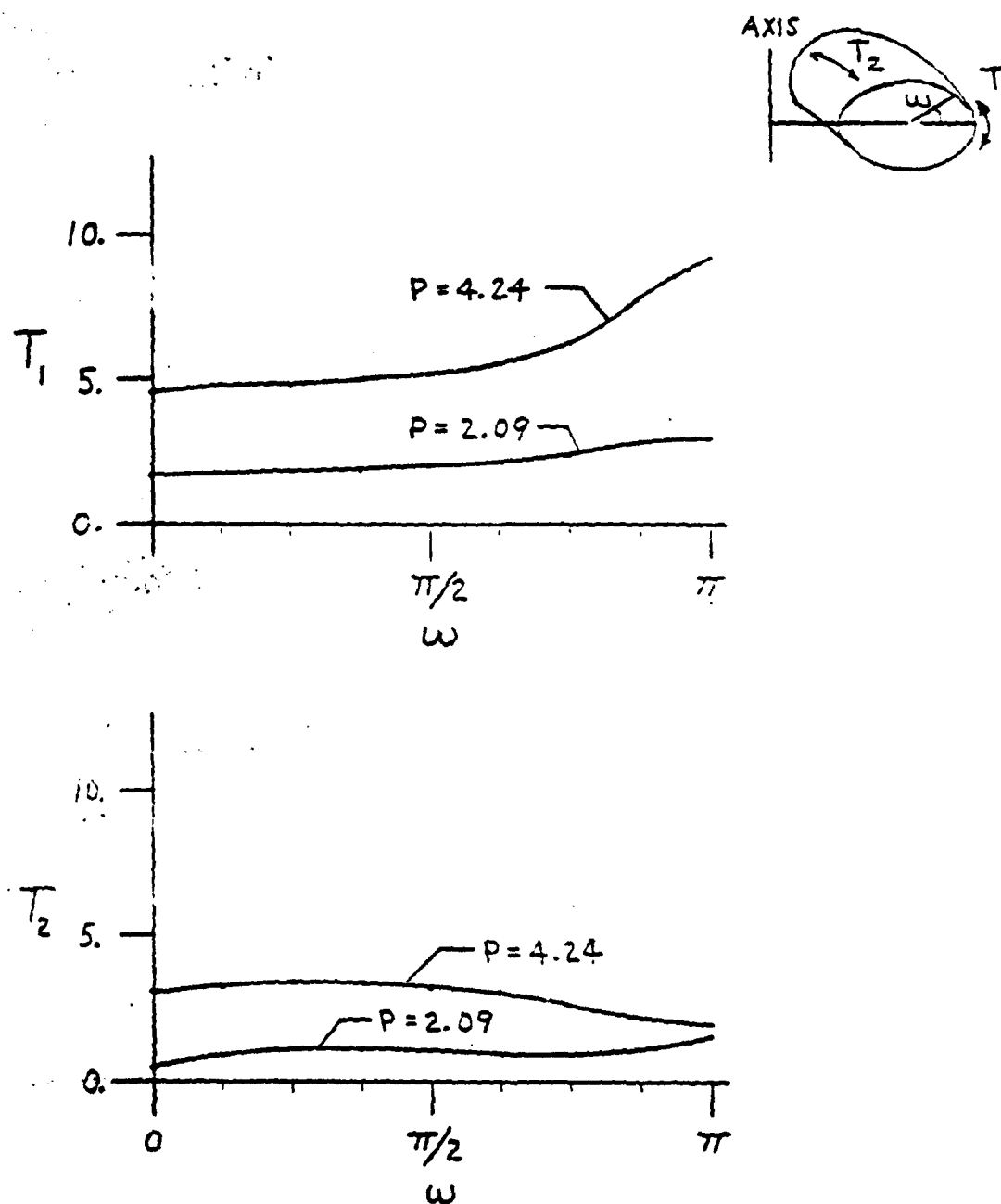TORUS WITH ELLIPTICAL
CROSS SECTION.

FIGURE 5.14   STRESS RESULTANTS, TORUS
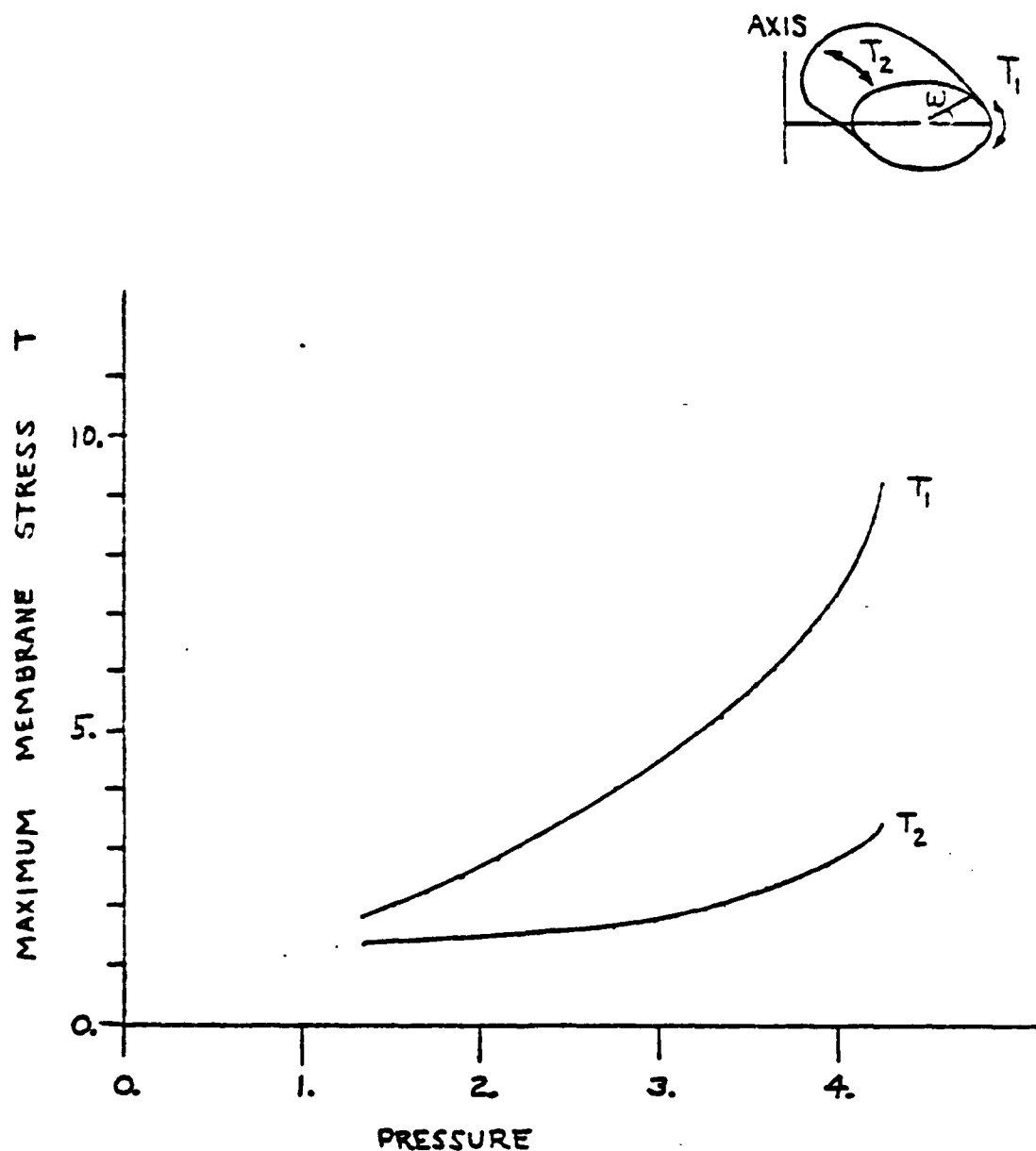WITH ELLIPTICAL CROSS
SECTION.

FIGURE 5.15 MAX MEMBRANE STRESS VS PRESSURE, TORUS WITH ELLIPTICAL CROSS SECTION.

REFERENCES

1. Treloar, L. R. G., <u>The Physics of Rubber Elasticity</u>, second
   edition, Oxford University Press, 1958.

2. Green, A. E., and Zerna, W., <u>Theoretical Elasticity</u>, Oxford
   University Press, 1963, page 76.

3. Levinson, M., "The Application of the Principle of Stationary
   Potential Energy to Some Problems in Finite Elasticity,"
   Journal of Applied Mechanics, Vol 87, series E, 1965, pp656-660.

4. Oden, J. T., <u>Finite Elements of Nonlinear Continua</u>, McGraw-Hill
   Book Co., 1972, page 223.

5. Cescotto, S., and Fonder, G., "A Finite Element Approach for Large
   Strains of Nearly Incompressible Rubber-Like Materials," Int. J.
   Solids Structures, Vol 15, pp 589-605, 1979.

6. Oden, J. T., and Key, J. E., "On the Effect of the Form of the
   Strain Energy Function on the Solution of a Boundary-Value Problem
   in Finite Elasticity," Computers & Structures, Vol 2, 1972, pp
   585-592.

7. Tielking, J. T., and Feng, W. W., "The Application of the Minimum
   Potential Energy Principle to Nonlinear Axisymmetric Membrane Prob-
   lems," Journal of Applied Mechanics, June 1974, pp 491-496.

8. Strang, G., and Fix, G., <u>An Analysis of the Finite Element Method</u>,
   Prentice-Hall, Inc., 1973.

9. Fried, I., "Numerical Integration in the Finite Element Method,"
   Computers and Structures, Vol 4, 1974, pp 921-932.

REFERENCES CONTINUED

10. Fried, I., "Discrete Integration in Nonlinear Finite Element Analysis," 1979.

11. Matthies, H., and Strang, G., "The Solution of Nonlinear Finite Element Equations," Int. J. for Numerical Methods in Engineering, Vol 14, 1979, pp 1613-1626.

12. Rivlin, R. S., and Thomas, A. G., "Large Elastic Deformations of Isotropic Materials VIII, Strain Distribution around a Hole in a Sheet," Phil. Trans. R. Soc., Section A, 1951, pp 289-298.

13. Verma, P.D.S., and Rana, O. H., "Radial Deformation of a Plane Sheet Containing a Circular Hole or Inclusion," Int. J. Nonlinear Mechanics, Vol. 13, 1978, pp 223-232.

14. Oden, J. T., "Numerical Formulation of Nonlinear Elasticity Problems," J. Struct. Div. ASCE, Vol. 93, No. ST3, 1967, pp 235-255.

15. Adkins, J. E., and Rivlin, R. S., "Large Elastic Deformations of Isotropic Materials, IX the Deformation of Thin Shells," Phil. Trans. R. Soc., Section A, 1952, pp 505-531.

16. Green, A. E., and Adkins, J. E., _Large Elastic Deformations and Non-linear Continuum Mechanics_, Oxford University Press, 1960, pp 152-160.

17. Love, A. E. H., _A Treatise on the Mathematical Theory of Elasticity_, 4th edition, Dover Publications, 1944, section 331.

18. Yang, W. H., and Feng, W. W., "On Axisymmetrical Deformations of Nonlinear Membranes," Journal of Applied Mechanics, Vol. 37, 1970, pp 1002-1011.

REFERENCES CONTINUED

10. Fried, I., "Discrete Integration in Nonlinear Finite Element Analysis," 1979.

11. Matthies, H., and Strang, G., "The Solution of Nonlinear Finite Element Equations," Int. J. for Numerical Methods in Engineering, Vol 14, 1979, pp 1613-1626.

12. Rivlin, R. S., and Thomas, A. G., "Large Elastic Deformations of Isotropic Materials VIII, Strain Distribution around a Hole in a Sheet," Phil. Trans. R. Soc., Section A, 1951, pp 289-298.

13. Verma, P.D.S., and Rana, O. H., "Radial Deformation of a Plane Sheet Containing a Circular Hole or Inclusion," Int. J. Nonlinear Mechanics, Vol. 13, 1978, pp 223-232.

14. Oden, J. T., "Numerical Formulation of Nonlinear Elasticity Problems," J. Struct. Div. ASCE, Vol. 93, No. ST3, 1967, pp 235-255.

15. Adkins, J. E., and Rivlin, R. S., "Large Elastic Deformations of Isotropic Materials, IX the Deformation of Thin Shells," Phil. Trans. R. Soc., Section A, 1952, pp 505-531.

16. Green, A. E., and Adkins, J. E., _Large Elastic Deformations and Non-linear Continuum Mechanics_, Oxford University Press, 1960, pp 152-160.

17. Love, A. E. H., _A Treatise on the Mathematical Theory of Elasticity_, 4th edition, Dover Publications, 1944, section 331.

18. Yang, W. H., and Feng, W. W., "On Axisymmetrical Deformations of Nonlinear Membranes," Journal of Applied Mechanics, Vol. 37, 1970, pp 1002-1011.

REFERENCES CONTINUED

19. Argyris, J. H., Balmer, H., Doltsinis, J., Dunne, P., Hasse, M.,
    Müller, M., and Scharpf, D., "Finite Element Method - The Natural
    Approach," Computer Methods in Applied Mechanics and Engineering
    17/18 (1979), pp 1-106.

20. Jordan, P. Fr., "Stresses and Deformations of the Thin-Walled
    Pressurized Torus," J. Aerospace Sci. 29, 1962, pp 213-225.

21. Sanders, J. L., and Liepins, A. A., "Toroidal Membrane under
    Internal Pressure," AIAA J., Vol. 1, 1963, pp 2105-2110.

22. Liepins, A. A., "Free Vibrations of Prestressed Toroidal Mem-
    brane," AIAA J., Vol. 3, 1965, pp 1924-1933.

23. Kydoniefs, A. D., and Spencer, A. J. M., "The Finite Inflation of
    an Elastic Torus," Int. J. Engng Sci., Vol. 3, 1965, pp 173-195.

24. Kydoniefs, A. D., and Spencer, A. J. M., "The Finite Inflation of
    an Elastic Toroidal Membrane of Circular Cross Section," Int. J.
    Engng. Sci., Vol. 5, 1967, pp 367-391.

19a. Young W. H.. "Stress Concentration in a Rubber Sheet Under
    Axially Symmetric Stretching." Journal of Applied Mechanics,
    Vol. 34, 1967, pp 942-946.

LMED

8